Inorganic Chemistry
Cite This: Inorg. Chem. XXXX, XXX, XXX−XXX
Article
pubs.acs.org/IC

Investigations of the Magnetic and Spectroscopic Properties of V(III) and V(IV) Complexes

Casey Van Stappen,[†] Dimitrios Maganas,[‡] Serena DeBeer,[†] Eckhard Bill,[‡] and Frank Neese*[,‡]

[†]Max-Planck Institute for Chemical Energy Conversion, Stiftstrasse 34-36, Mülheim an der Ruhr, 45470 North Rhine-Westphalia, Germany

[‡]Max-Planck-Institüt für Kohlenforschung, Kaiser-Wilhelm-Platz 1, Mülheim an der Ruhr, 45470 North Rhine-Westphalia, Germany

Supporting Information

ABSTRACT: Herein, we utilize a variety of physical methods including magnetometry (SQUID), electron paramagnetic resonance (EPR), and magnetic circular dichroism (MCD), in conjunction with high-level ab initio theory to probe both the ground and ligand-field excited electronic states of a series of V(IV) ($S = {}^1/_2$) and V(III) ($S = 1$) molecular complexes. The ligand fields of the central metal ions are analyzed with the aid of ab initio ligand-field theory (AILFT), which allows for a chemically meaningful interpretation of multireference electronic structure calculations at the level of the complete-active-space self-consistent field with second-order N-electron valence perturbation theory. Our calculations are in good agreement with all experimentally investigated observables (magnetic properties, EPR, and MCD), making our extracted ligand-field theory parameters realistic. The ligand fields predicted by AILFT are further analyzed with conventional angular overlap parametrization, allowing the ligand field to be decomposed into individual σ- and π-donor contributions from individual ligands. The results demonstrate in VO^{2+} complexes that while the axial vanadium−oxo interaction dominates both the ground- and excited-state properties of vanadyl complexes, proximal coordination can significantly modulate the vanadyl bond covalency. Similarly, the electronic properties of V(III) complexes are particularly sensitive to the available σ and π interactions with the surrounding ligands. The results of this study demonstrate the power of AILFT-based analysis and provide the groundwork for the future analysis of vanadium centers in homogeneous and heterogeneous catalysts.

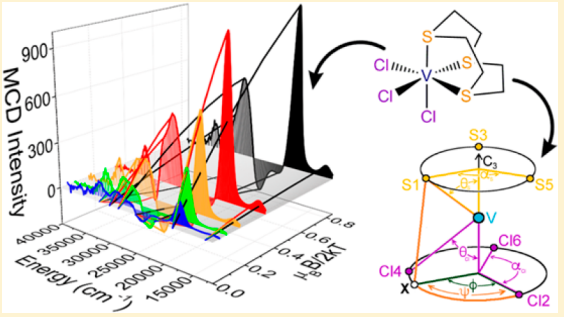

1. INTRODUCTION

Vanadium (V) is an abundant and widely distributed element that plays a critical role in both biology and modern catalysis,[1,2] where its ability to access a variety of oxidation states lends itself to applications requiring either oxidizing or reducing behavior. Industrially, the oxidative capabilities of V_2O_5 are exploited in several critical processes, including the synthesis of sulfuric acid, maleic and phthalic anhydride,[3−5] and the decomposition of the NO_x species responsible for acid rain.[6] Additionally, great interest has arisen in recent decades toward the use of vanadium oxide catalysts for the selective oxidative−dehydrogenation of short alkanes.[7−15] Biologically, vanadium is found in marine-haloperoxidases,[16] amavadin,[17] vanadium nitrogenase,[18,19] and other organisms spanning a range of oxidation states from V(III) to V(V).[20,21] In many of these systems, the active vanadium species still remains controversial. Therefore, developing ways to understand the electronic and geometric structures of vanadium in such environments remains critical to the development and improvement of these applications.

Despite the intensive efforts present in the literature to understand vanadium ions in their many facets, the number of studies set forth to understand the spectroscopic and magnetic properties of molecular vanadium complexes has remained relatively limited, particularly since the 1970s. More specifically, only a handful of examples exist that have utilized magnetic circular dichroism (MCD) to probe these properties.[22,23] This is especially surprising in the case of V(IV) because the $S = {}^1/_2$ ground state should provide relatively simple and easily interpreted spectra in the frame of a one-electron picture. Even so, there is only one reported study that describes the C terms of complexes bearing a VO^{2+} core.[23] Similarly, only a single report has been made that utilizes MCD as a probe of V(III).[22]

Herein, we present our investigation of the ground- and excited-state electronic properties of vanadium in the V(IV) and V(III) oxidation states. More specifically, we investigate the optical and magnetic properties of V(IV) and V(III) in a series of coordination environments, as shown in Figure 1. The V(IV) complexes all employ acetyl acetonate ($acac^-$) as an equatorial ligand, with this series consisting of $VO(acac)_2$ (**1**), $VO(acac)_2$nPrCN (**2**), $VO(acac)_2$Py (**3**), and $VCl_2(acac)_2$ (**4**). These particular complexes were selected to represent both vanadyl (**1**−**3**) and "bare", also known as nonoxo (**4**), vanadium species in 5- and 6-coordinate environments. Since

Received: February 22, 2018

DOI: 10.1021/acs.inorgchem.8b00486
Inorg. Chem. XXXX, XXX, XXX−XXX

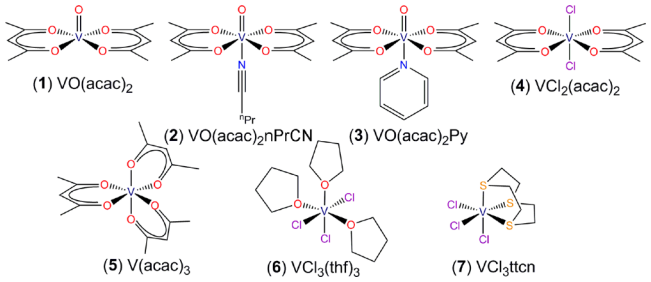

Figure 1. Vanadium complexes under investigation.

V(III) is most commonly found in an octahedral environment, the $V(acac)_3$ (**5**), $VCl_3(thf)_3$ (**6**), and VCl_3ttcn (**7**) complexes were selected to provide both a variety of octahedral distortions and ligand-field environments. Magnetic susceptibility, electron paramagnetic resonance (EPR), and variable-temperature variable-field magnetic circular dichroism (VTVH-MCD) techniques are used to investigate the ground-state electronic properties of the outlined complexes, while absorption [UV–vis/near-IR (NIR)] and MCD spectroscopies are used to probe excited electronic states. To provide further insight into the electronic structures of these complexes, high-level ab initio theory has been employed in the form of the complete-active-space self-consistent-field method in conjunction with N-electron valence perturbation theory (CASSCF/NEVPT2).

2. METHODS

2.1. Complexes and Models. Compound **1** was purchased from Sigma-Aldrich and used to generate complex **2** in the presence of butyronitrile (nPrCN). Complexes **3**–**7** were synthesized according to literature methods.[24−29] Further details regarding the synthesis and crystallographic data of complexes **1** and **2** are provided in the Supporting Information. Renderings of the available crystal structures of these complexes are provided in Figure D1.

2.2. Magnetic Measurements. Bulk magnetization measurements were performed for the V(III) complexes using a Quantum Design MPMS-7 SQUID magnetometer, calibrated with a standard palladium reference sample (error < 2%). All samples consisted of randomly oriented microcrystals, with total masses of 18.1 mg for **5**, 25.4 mg for **6**, and 30.40 mg for **7**, which were placed in anaerobic quartz-glass holders for measurement. Minute amounts of eicosane (melting point of 310 K) were used to prevent torqueing of the material under large applied magnetic fields. The temperature dependence of the magnetic susceptibility was measured from 2 to 290 K at a magnetic field of 0.1 T. Magnetization versus field measurements were performed at multiple temperatures at magnetic fields of 1, 4, and 7 T over a range of 2–260 K. Blank measurements of the quartz-glass holder were performed for background subtraction. Desired magnetization data were acquired by fitting amplitudes from the appropriately corrected SQUID response curves. Values for the sample magnetization were divided by the number of moles and converted to units of molar susceptibility using the definition $\chi = \mu_B M/B$. Values of χ were then corrected for any temperature-independent paramagnetism or underlying diamagnetism by the use of tabulated Pascal's constants. The temperature-dependent magnetic susceptibility and field-dependent magnetization data were handled and simulated using the *julX* and *julX_2S* software packages, which employ the spin Hamiltonian described by eq 1 to calculate true powder averages in three dimensions, assuming the presence of an isolated spin ground state and collinear D and g matrixes, where the **g** matrix may be isotropic, axial, or rhombic.

$$H = D[S_z^2 - S(S+1)/3 + (E/D)(S_x^2 - S_y^2)] + \mu_B \cdot \mathbf{B} \cdot g \cdot S \quad (1)$$

Since D may be either positive or negative, values on both sides were explored. The value of E was constrained such that $|E| < |D/3|$. An averaged, isotropic **g** tensor (g_{av}) was employed in all modeling, in which $g_{av} = \sqrt{\sum \frac{(g_i)^2}{3}}$. Values for E, D, and g were optimized by a least-squares minimization using data from all fields and temperatures simultaneously.

2.3. EPR Measurements. EPR measurements were recorded at temperatures of 30 K for complexes **1**–**3** using continuous-wave (cw) X-band EPR spectra recorded on a Bruker E500 ELEXSYS spectrometer equipped with a Bruker dual-mode cavity (ER4116DM) and an Oxford Instruments helium-flow cryostat (ESR 900). A high-sensitivity Bruker Super-X (ER-049X) bridge with an integrated microwave-frequency counter was employed as the microwave unit. A magnetic field controller (ER032T) was externally calibrated with a Bruker NMR field probe (ER035M). cw Q-band EPR measurements performed on complex **4** utilized a Bruker ESP-300E spectrometer with a Bruker Q-band cavity (ER5106QT) with a Bruker flexline support and an Oxford Instruments helium-flow cryostat (CF935). Microwave frequencies were calibrated using a Hewlett-Packard frequency counter (HP5352B), and the field control was calibrated using a Bruker NMR field probe (ER035M). Spectra were recorded on frozen solutions of complexes **1**–**3**, where **1** was dissolved in dichloromethane (DCM), **2** in nPrCN, and **3** in pyridine (Py). Spectra of **4** were recorded on a solid powder at 30 and 50 K in the X-band and Q-band experiments, respectively. X-band measurements utilized a 0.2 mW microwave power and 0.75 mT and 100 kHz modulation, while 0.1 mW microwave power and 0.01 mT modulation were used in Q-band measurements. Spectra were analyzed in both the local software package *esim_gfit* (available from E.B.) and the software package *EasySpin* (version 5.1.9), as implemented in *Matlab*.[30]

2.4. Optical and MCD Measurements. All presented optical measurements of all compounds, with the exception of **2**, were prepared as finely dispersed powders embedded in KBr. Because the coordination of nPrCN in $VO(acac)_2$nPrCN is not strong enough to form an isolable complex,[27] the presented samples for optical and EPR samples of **2** were made in a glassed nPrCN solution at concentrations of 2 and 1 mM, respectively. All samples, with the exception of **2**, were prepared in a strictly anaerobic, moisture-free glovebox. Electronic absorption and VTVH-MCD measurements were recorded using an OLIS DSM17 UV–vis/NIR CD spectropolarimeter in conjunction with an Oxford Instruments Spectromag SM4000 magnetocryostat over ranges of 2–80 K and fields of 1–7 T. Additional UV–vis/NIR absorption measurements were performed using a Cary 6000i UV–vis/NIR spectrophotometer in conjuction with an Oxford Instruments Optistat-DN cryostat at temperatures of 80 K. All low-temperature measurements were performed on samples prepared in MCD cells using either 0.1 or 0.3 mM quartz windows. MCD and electronic absorption data were analyzed using local software (developed by E.B. at the MPI-KOFO, Mülheim an der Ruhr, Germany). MCD spectra were fit simultaneously by a number of Gaussians as a function of the temperature and field dependence in conjunction with their corresponding 80 K UV–vis/NIR spectrum. Spectra were analyzed using the global fitting procedure in the program *BF*, with a bandwidth restriction whereby the largest bandwidth was not allowed to vary higher than ∼2 times the smallest bandwidth measured for a given compound; exceptions to this approach are noted where applicable.

To probe the magnetic and polarization properties of the observed C terms, VTVH-MCD measurements were performed by measuring the MCD intensity at a fixed wavelength for varying fields at multiple temperatures. The resulting isotherms of the MCD intensity are present as a function of $\mu_B B/2kT$, where μ_B is the Bohr magneton, B is the strength of the applied magnetic field, k is the Boltzmann constant, and T is the temperature (K). It has been shown that the saturation behavior of systems with $S > {}^1/_2$ depends on a combination of the spin-Hamiltonian parameters and transition polarizations, allowing insight into the properties of both the ground and excited states.[31] Using the equation for the orthorhombic approximation,

DOI: 10.1021/acs.inorgchem.8b00486
Inorg. Chem. XXXX, XXX, XXX–XXX

$$\frac{\Delta\varepsilon}{E} = \frac{\gamma}{4\pi S}\int_0^{\pi}\int_0^{2\pi}\sum_i N_i(l_x\langle S_x\rangle_i M_{yz}^{\mathrm{eff}} + l_y\langle S_y\rangle_i M_{xz}^{\mathrm{eff}} + l_z\langle S_z\rangle_i M_{xy}^{\mathrm{eff}})\sin\theta\,\mathrm{d}\theta\,\mathrm{d}\phi r \quad (2)$$

as implemented in the local program *mcd3D_2S* (available from E.B.), global fittings of the recorded VTVH magnetization curves were simulated. In this equation, $\Delta\varepsilon/E$ is the MCD intensity, γ represents a collection of constants, S is the total spin of the ground state, N_i is the Boltzmann population of the ith magnetic sublevel of the electronic ground state, $l_{x,y,z}$ are the directional cosines of the spin Hamiltonian, and $\langle S_{x,y,z}\rangle_i$ are the expectation values of the x, y, and z components of the spin operator S over the ith magnetic eigenstate, respectively. For complexes **5** and **6**, VTVH-MCD curves were fit using several sets of spin-Hamiltonian parameters, including those determined in the present study by magnetic susceptibility measurements and those previously reported from high-field EPR (HFEPR) studies by Krzystek and co-workers.[22] Similarly, the VTVH-MCD curves of **7** were fit in several sets using the spin-Hamiltonian parameters, as determined by magnetic susceptibility (presented here) and previous HFEPR measurements.[22] The polarization factors M_{vw}^{eff} (v, w = x, y, z) are effective transition dipole moments, which are independently determined for each transition. Using these, the individual polarization of a given MCD band may be calculated using the relationship

$$\%\,x = 100 \times \frac{(M_{xy}^{\mathrm{eff}}M_{xz}^{\mathrm{eff}})^2}{(M_{xy}^{\mathrm{eff}}M_{xz}^{\mathrm{eff}})^2 + (M_{xy}^{\mathrm{eff}}M_{yz}^{\mathrm{eff}})^2 + (M_{xz}^{\mathrm{eff}}M_{yz}^{\mathrm{eff}})^2} \quad (3)$$

for the percentage of x polarization and the complementing permutations for the corresponding percentage y and z components.

2.5. Computational Details. All calculations were performed using the quantum computing suite *ORCA 4.0*.[32] Because the recorded spectra were performed on solid complexes, it was natural to utilize the originally reported crystal structures, with optimization steps only being performed for hydrogen atoms. Geometry optimizations of hydrogen atoms were performed at the level of density functional theory with the pure exchange correlation functional BP86, which utilizes Becke's 1988 exchange functional along with the gradient corrections of Perdew as well as Perdew's 1981 local correlation functional,[33,34] in conjunction with the second-definition triple-ζ valence-polarized (def2-TZVP) basis of Alrich and co-workers and the complementing *def2/J* auxiliary basis set.[35,36]

The initial structures for complexes **3**−**7** were obtained from the reported crystallographic structures.[29,37−40] Because of the lack of an axially unperturbed crystal structure of **1**, the influence of proximal ligation to **1** was investigated through the generation of a clear series of models based on the $VO(acac)_2Py$ crystal structure **3**. To this end, four models were generated that involve the presence/absence of the Py ligand and its trans effect on the V═O bond. These model structures include (a) $VO(acac)_2$ (**1a**), generated by the simple removal of Py from the $VO(acac)_2Py$ structure, with no further structural modifications, (b) $VO(acac)_2$ (**1b**) again generated by the removal of Py from $VO(acac)_2Py$, but with the V═O bond length shortened from 1.573 to 1.543 Å and no further optimization steps, (c) $VO(acac)_2Py$ (**3a**), and (d) $VO(acac)_2Py$ (**3b**), with the V═O bond length shortened from 1.573 to 1.543 Å (**3b**). The combination of these four models allows us to look individually at the influences of the Py coordination and V═O bond length on the ligand-field manifold of these complexes.

Calculations of the ground- and excited-state properties, including MCD, were performed using the complete-active-space self-consistent-field method with consideration of spin−orbit coupling (SOC-CASSCF)[41,42] in conjunction with N-electron valence perturbation theory to second order (NEVPT2)[43,44] in order to recover missing dynamic electron correlation. These calculations were performed using the triple-ζ atomic natural orbital basis *ano-pVTZ*[45] along with the *AutoAux* basis[46] option of *ORCA*, in conjuction with second-order Douglas−Kroll−Hess (DKH2) to account for scalar relativistic effects. SOC was treated through the mean-field (SOMF) approximation,[47,48] and the effective Hamiltonian approach[49−51] was used to compute the spin-Hamiltonian parameters. In order to accurately model the ligand-field structure of the V(III) and V(IV) complexes, active spaces were chosen to encompass the dominate bonding/antibonding orbitals formed between vanadium and the surrounding ligand. A total size of (9,9) was used for complexes **1**−**4** with a minimum of 5 doublet roots to describe the ligand-field excited states. Active spaces of (12,10) along with 10 triplet roots and 15 singlet roots were selected for the V(III) series **5**−**7**. Additionally, minimal active spaces of (2,5) and (1,5) were calculated for all V(III) and V(IV) complexes, respectively, to investigate the significance of including of bonding orbitals in these calculations. AILFT analysis[52,53] was requested by canonicalizing the active orbitals in a specific manner (keyword actorbs = dorbs in *ORCA*).

2.6. Ligand-Field Analysis. The program *AOMX* was utilized for the analysis of all data in terms of ligand-field parameters.[54] *AOMX* calculates the d^n electron terms in the framework of either the crystal field or angular overlap model (AOM).

The ability to fully determine the ligand-field parameters of a given complex experimentally is highly dependent on the number of available observable electronic transitions and choice of their assignment. In practice, one is typically limited to a low-energy subset of spin-allowed ligand-field transitions, such that the problem usually requires more parameters than can be determined by the available information. Meanwhile, calculations are capable of providing all ligand-field states of interest. The discrepancy in the available information has often led to considerable disagreement between the calculated and experimentally determined parameters. In particular, a lower number of experimental points require a greater number of assumptions to be made in the applied interpretive model. Therefore, ligand-field parameters determined from CASSCF/NEVPT2 calcu-

Scheme 1. Descriptive Angles of (a) V(IV) Complexes, (b and c) $V(acac)_3$, and (d and e) VCl_3ttcn[a]

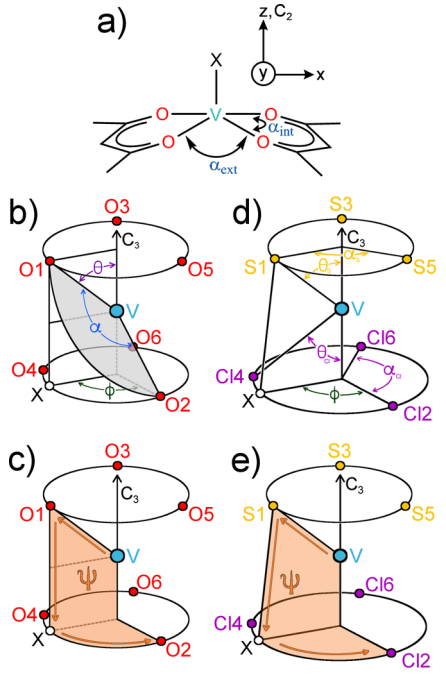

[a]In parts b and c, θ is defined as the angle between the unique C_3 axis, the central V, and the coordinating ligand atom. In part b, α is defined by the chelating ligand bite angle, while in part c, it is used to describe the angle between ligands that lie in-plane orthogonal to the unique C_3 axis. The projection "X", which lies in-plane with the C_3 axis and a coordinating ligand, is needed to help describe ψ and ϕ. Here, ϕ describes the twist angle between the projection X and a component ligand in the C_3 orthogonal plane, while ψ describes the dihedral angle V−L−X−(L + 1) (for example, in part b, V−O1−X−O2).

DOI: 10.1021/acs.inorgchem.8b00486
Inorg. Chem. XXXX, XXX, XXX−XXX

lated excited states were derived by using both (a) all calculated ligand-field states and (b) an "abbreviated" number of excited states to match those assigned experimentally.

3. GEOMETRIC STRUCTURE

Embedding V(IV) in an equatorial bis(acac$^-$) environment generates a pseudo-C_{4v}-symmetric complex (within the first coordination sphere), as depicted in Scheme 1a. At present, we define the primary z axis to run along the V−X bond, with the xz plane bisecting the two acac$^-$ ligands and the yz plane bisecting between the acac$^-$ ligands. In complex **3**, for which the crystal structure is known, the vanadium sits above the equatorial plane ($\angle$X−V−O = 100°) such that the internal bite angle (α_{int}) of the acac$^-$ ligands is ∼89° and that between either acac$^-$ (α_{ext}) is ∼87°. Meanwhile in complex **4**, vanadium actually sits within the equatorial plane (average $\angle$X−V−O = 90°), leading to an internal bite angle of 86.6° and an external bite angle of 93.4°. Therefore, while ligation of acac$^-$ implies that these complexes are strictly either C_{2v} (**1**−**3**) or D_{2h} (**4**) symmetric in geometry, the relatively small differences between α_{int} and α_{ext} imply that these systems may behave as minor distortions from their respective higher-order counterparts, C_{4v} and D_{4h}.

Of the V(III) complexes, the trigonal distortion of tris-bidentate complexes such as **5** may be described in terms of the polar angle θ, twist angle ϕ, bite angle α, and dihedral angle ψ (Scheme 1b). In perfect octahedral symmetry, θ = 54.74°, ϕ = 60°, α = 90°, and ψ = 60°. In **5**, these angles average to θ = 54.4°, ϕ = 60°, α = 88°, and ψ = 43.5°. The significant decrease in ψ implies a considerable trigonal expansion in this complex. Meanwhile, while **7** is also trigonally distorted, the meridonal faces of the complex along the C_3 axis are no longer equal (Scheme 1c). This requires individual parameters for the polar angle θ and the angle α for each face. We find here that θ_{Cl} = 63.0°, θ_S = 49.5°, ϕ = 60°, α_{Cl} = 101°, α_S = 82°, and ψ = 61.0°. The combination of θ_{Cl} > 60° and α_{Cl} > 90° implies compression along the Cl2−Cl4−Cl6 face, while θ_S < 60° and α_S < 90° show elongation along the S1−S3−S5 face. Complex **6** can be described more simply in terms of several polar angles θ and dihedral angles ψ to describe the out-of-plane twists of the tetrahydrofuran (thf) ligands. The highest-order axis, which C_2, is oriented along the near-linear Cl−V−thf coordinate, giving θ_{Cl} = 92.5° and θ_{thf} = 93.4°. Two dihedral angles are needed to describe each the equatorial and axial thf ligands. The parameter ψ_{eq} describes deviations from the equatorial plane, while ψ_{ax} describes deviations from an axial plane containing the C_2 axis and all three Cl ligands. With these definitions, ψ_{eq} = 34.6° and ψ_{ax} = 43.3°.

4. ELECTRONIC STRUCTURE

Under the C_{4v} axially compressed distortion, the d manifold of V(IV) is split such that $b_2(d_{xy})$ < $e(d_{xz},d_{yz})$ < $b_1(d_{x^2-y^2})$ < $a_1(d_{z^2})$. The ligand fields of vanadyl complexes have classically been interpreted by the model developed by Ballhausen and Gray for $VO(H_2O)_5^{2+}$; here, the b_2 orbital is noninteracting with the surrounding ligand field, while the e, b_1, and a_1 orbitals overlap with the oxo-π, equatorial H_2O-σ, and oxo-σ orbitals, respectively.[55] In the present case, the equatorial σ interaction arises from the acac$^-$ ligand, as summarized in Scheme 2.

The electronic structure of the VO^{2+} center embedded within 5- and 6-coordinate complexes is a topic with considerable history.[6,56−64] Although heavily debated in the 1960s, the most popular model proposed by Ballhausen and Gray in 1961 is still

Scheme 2. (a) Orbital Overlap Scheme of V(IV) with O^{2-} and acac$^-$ Ligands To Form the $VO(acac)_2$ Complex with (b) Corresponding Orbitals[a]

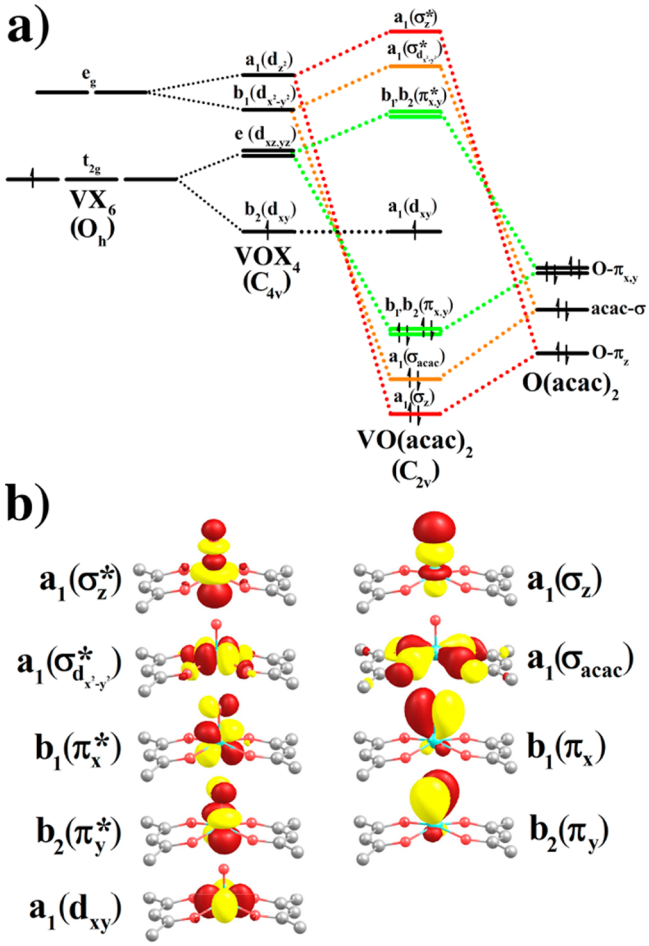

[a]Orbitals were generated using an isosurface value of 0.05.

prevailing.[55] This consists of a single unpaired electron of V(IV) predominately occupying the $3d_{xy}$ orbital and the $3d_{z^2}$ and $3d_{xz,yz}$ orbitals undergoing several strong interactions with the terminal oxo to form a highly covalent bond. While the ligation of acac$^-$ implies that these complexes are strictly either C_{2v} (**1**−**3**) or D_{2h} (**4**) symmetric, the axial distortion is usually considered to be the primary perturber, while the equatorial distortion is only a minor perturbation. Upon axial compression or elongation, the orbitals that are able to interact along the z axis will either increase or decrease in energy, respectively. Therefore, axial compression results in an approximate ordering of $3d_{xy}$ < $3d_{xz,yz}$ < $3d_{x^2-y^2}$ < $3d_{z^2}$, in which the relative ordering of $3d_{xz,yz}$ and $3d_{x^2-y^2}$ depends upon the degree of compression. Similarly, axial elongation is anticipated to result in a $3d_{xz,yz}$ < $3d_{xy}$ < $3d_{z^2}$ < $3d_{x^2-y^2}$ ordering. In turn, the ^{2}D free-ion state of a d^1 system, which is split into the $^2T_{2g}$ ground state and ^2E_g excited state in the presence of an O_h field, will be further split in C_{4v} under an axial compression to $^2B_2$ < ^2E < $^2B_1$ < $^2A_1$, while axial elongation in D_{4h} results in ^2E_g < $^2B_{2g}$ < $^2A_{1g}$ < $^2B_{1g}$ (Figure D2).

V(III) presents a d^2 system (S = 1), in which the ^{3}F and ^{3}P free-ion states are split to form a $^3T_1(F)$ ground state and $^3T_2(F)$, $^3T_1(P)$, and $^3A_2(P)$ excited states in an octahedral environment. The addition of trigonal distortion (as in

DOI: 10.1021/acs.inorgchem.8b00486
Inorg. Chem. XXXX, XXX, XXX−XXX

complexes **5** and **7**) lowers the effective symmetry to D_3/C_{3v}, further splitting the triplet states from $^3T_1 \rightarrow {}^3A_2$, ^3E and $^3T_2 \rightarrow {}^3A_1$, ^3E (described in Figure D3). For even larger distortions, such as in the meridonal complex **6** with C_2 symmetry, all degeneracy is lost.

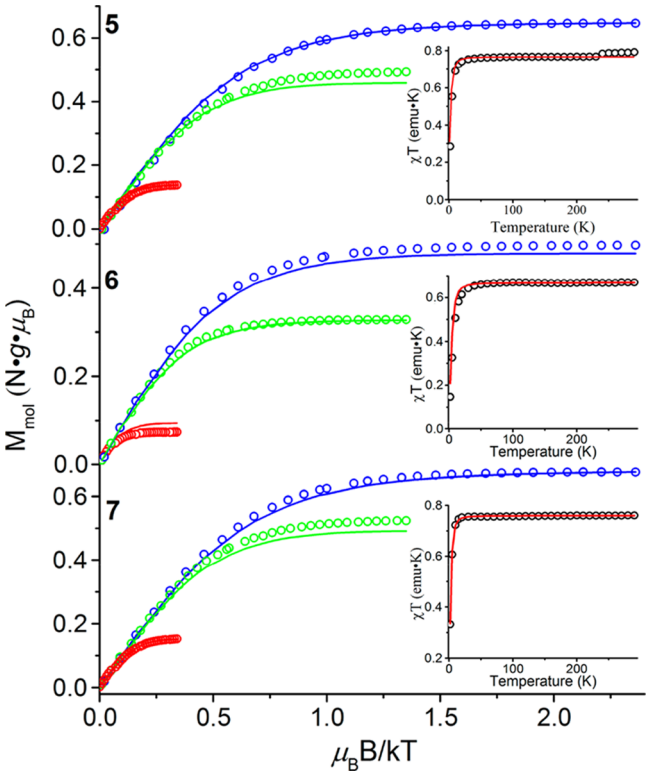

Figure 2. Temperature and field dependence of the molar magnetization and magnetic susceptibilities (insets) of complexes **5**−**7**. Solid lines represent the $S = 1$ simulated spin Hamiltonians. Multifield measurements of the molar magnetization were performed at 7 T (blue), 3 T (green), and 1 T (red). Magnetic susceptibilities were measured at 0.1 T.

5. RESULTS AND ANALYSIS

5.1. Magnetic Susceptibility Measurements. Variable-temperature variable-field direct-current SQUID measurements were performed for complexes **5**−**7** in order to determine their magnetic ground-state characteristics. The fit effective magnetic moment and magnetization curves are presented in Figure 2. The χT values for all three V(III) complexes decrease drastically below 50 K, indicating the presence of zero-field-splitting (ZFS) effects.[65] Susceptibility and magnetization data were fit simultaneously, and the resulting spin-Hamiltonian parameters are presented in Table 1 along with literature values for reference.

For **5**, reasonable fits were achieved with positive values of D ranging from 6.9 to 8 cm^{-1} and $g_{av} = 1.75$. These values are in good agreement with those reported previously by both Krzystek et al.[22] and Gregson et al.[66] Similarly, reasonable fits of **7** were only achievable using positive D with a value of 6.1 cm^{-1}. Notably, values of E/D for **7** were quite flexible with little perturbation to the fit across a range of 0−0.1; however, values closer to zero were still favored. Simulations of **6** proved to be somewhat more difficult; using $g_{av} = 1.7$ and $E/D = 0.33$, magnetic susceptibility data favor $|D| = 14$−15 cm^{-1}, while simulations of the magnetization data favor $|D| = 10$ cm^{-1}.

Table 1. Spin-Hamiltonian Parameters of V(III) Complexes 5−7 As Simulated for the Present Magnetic Susceptibility/Molar Magnetization and VTVH-MCD Measurements[a]

compound	method	$g_\perp$	$g_\parallel$	D (cm^{-1})	E/D
5	magn.	1.75	1.75	6.9	0.132
	VTVH-MCD	1.75	1.75	7.1	0.14
	SOC-C/N	1.73, 1.75	1.94	9.6	0.06
	HFEPR[b]	1.833(4), 1.72(2)	2.03(2)	7.470(1)	0.256
	magn.[b]	1.7	1.7	7.4	0.324
6	magn.	1.7	1.7	10−14	0.33
	VTVH-MCD	1.85	1.85	10	0.33
	SOC-C/N	1.59, 1.69	1.95	16.2	0.18
	HFEPR[b]			11.85	0.33
	magn.[b]	1.7	1.7	11−15	0.33
	VTVH-MCD[b]	1.8	1.8	−10	0.16
7	magn.	1.77	1.77	6.1	0−0.1
	VTVH-MCD	1.8	1.8	6.1	0.0
	SOC-C/N	1.73, 1.75	1.93	9.5	0.06

[a]Additionally, the SOC-CASSCF(12,10)/NEVPT2 (abbreviated as SOC-C/N)-calculated parameters are provided. [b]Literature values previously determined by HFEPR and magnetization simulations are also included.[22]

5.2. EPR Measurements. *5.2.1. X-Band EPR Spectroscopy of the VO(acac)$_2$ Series.* The X-band EPR spectra of complexes **1**−**3** measured on frozen solutions in DCM, nPrCN, and Py, respectively, display the typical eight-line pattern of vanadium, which has a nuclear spin of $I = {}^7/_2$ (natural abundance of ^{51}V = 99.8%).[67] A high degree of agreement between the simulation and experiment is found for all spectra, which are presented in Figure 3 along with corresponding simulated parameters of the $S = {}^1/_2$ spin Hamiltonian in Table 2. The resulting simulations imply a small degree of orthorhombicity in the Zeeman splitting and hyperfine interaction tensors g and A. All fit **g** tensors appear relatively close to that of the free electron, implying well-isolated ground states in all three complexes.

The directionally dependent g tensor may be approximated using the rotational relationships of the real d orbitals and the equation

$$g_i = g_e\left(1 + \frac{n_i\zeta}{2S\Delta_i}\right) \quad (4)$$

where S is the total spin, g_e is the g value of the free electron, and $n_x = (id_{xz})^2$, $n_y = (-id_{yz})^2$, and $n_z = (-2id_{x^2-y^2})^2$. Therefore, $g_x = g_e - \zeta/S\Delta_x$, $g_y = g_e - \zeta/S\Delta_y$, and $g_x = g_e - 4\zeta/S\Delta_z$. Because the one-electron SOC constant is necessarily positive, this equation predicts that all principle g values will be smaller than that of the free electron and that $\Delta_{x,y,z}$ corresponds to the energy differences between the $3d_{xy}$ and $3d_{xz}$, $3d_{yz}$, and $3d_{x^2-y^2}$, orbitals, respectively. From eq 4, it is also notable that, as $\Delta_{x,y,z}$ increases, g_i approaches g_e, implying an increase in electronic isolation of the ground state.

Despite clear visual differences in the spectra, only minute variations in the simulated g-tensor values are found. We have assigned the spectral features such that $g_z < g_y < g_x$; upon moving from **1** to **3**, g_x decreases slightly while g_y increases,

DOI: 10.1021/acs.inorgchem.8b00486
Inorg. Chem. XXXX, XXX, XXX−XXX

Table 2. Summary of Spin-Hamiltonian Parameters of 1−4

compound/model	solvent	g_x	g_y	g_z	A_x	A_y	A_z
1	DCM	1.983	1.975	1.950	166.6	175.8	497.9
2	nPrCN	1.982	1.977	1.949	164.0	184.6	505.6
3	Py	1.982	1.981	1.947	171.2	184.8	500.4
4	solid	1.984	1.943	1.807			
1a		1.975	1.976	1.933			
1b		1.976	1.977	1.933			
3a		1.976	1.974	1.931			
3b		1.978	1.979	1.932			
4		1.928	1.843	1.736			

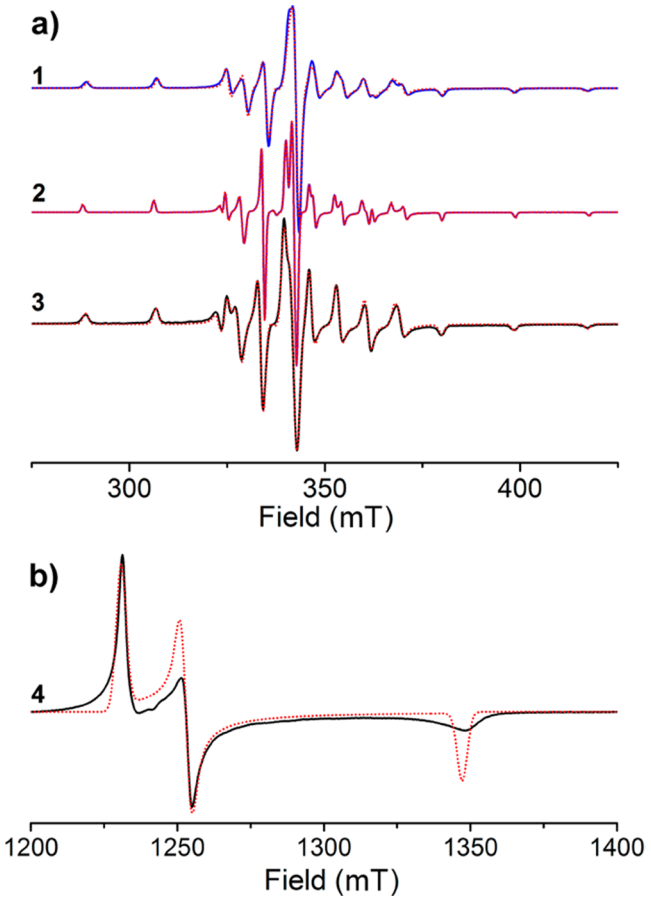

Figure 3. (a) Frozen-solution X-band EPR (solid) and simulated (red dot) spectra of **1** in DCM, **2** in nPrCN, and **3** in Py. Spectra were acquired at 30 K and 9.63 GHz using a power of 0.2 mW and a 7.46 G modulation amplitude. All samples were prepared at a 1 mM concentration. (b) Powder Q-band EPR (solid line) and simulated (red dot line) spectra of complex **4** acquired at 40 K and 34.08 GHz using a power of 0.01 mW and a 0.97 G modulation amplitude.

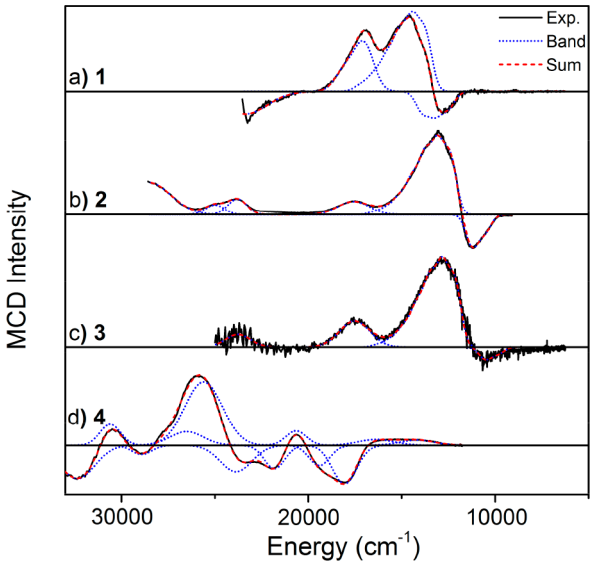

Figure 4. Gaussian-deconvoluted MCD spectra of (a) powder **1** in KBr, (b) **2** (1 mM) in nPrCN, (c) powder **3** in KBr, and (d) powder **4** in KBr. The presented spectra were obtained at 2 K and 5 T. The presented band deconvolutions were acquired through the simultaneous fitting of temperature- and field-dependent series in which the peak positions and bandwidths were fixed, allowing only the intensities to vary between measurements; this includes the fitting of measurements at 2, 5, 10, 20, and 40 K for a field of 5 T and fields of 3, 5, and 7 T at a temperature of 5 K.

becoming nearly equivalent in complex **3**. These changes result from the coordination of an axial ligand to the VO^{2+} core in complexes **2** and **3**, which results in a more axially symmetric coordination environment.

5.2.2. Q-Band EPR Spectroscopy of 4. Powder X-band measurements of **4** resulted in a relatively broad, axial $S = {}^1/_2$ signal. To better resolve this spectrum, powder Q-band EPR measurements of **4** were performed, as provided in Figure 3b, with the corresponding simulated spin-Hamiltonian parameters in Table 2. Complex **4** presents a distorted axial spectrum that supports the presence of a low-lying ligand-field excited state at ∼1000 cm^1, according to eq 4.

5.3. Optical and MCD Measurements. *5.3.1. V(IV) Complexes.* The deconvoluted MCD spectra of complexes **1**−**4** are presented in Figure 4, with the corresponding fit components presented in Table 3 and the absorption spectrum in Figure D4. Interpretation of the spectra was achieved through the application of a quantitative Gaussian deconvolution of both temperature- and field-dependent series for each complex using a minimum set of bands, which were fixed in energy and bandwidth for all fields and temperatures, with only the intensity allowed to vary. In particular, a set of 4 bands were used for complexes **1** and **3**, 6 for complex **2**, and 12 for complex **4**.

5.3.1.1. VO^{2+} Complexes (1−3). The lower-energy spectral region of complexes **1**−**3** (Figure 4) shows three distinct features between 5000 and 20000 cm^{-1}, beginning with a small negative dip at lower energy, followed by a more intense positive band to form a quasi-derivative shape. This is followed by a second positive feature that appears between 17000 and

DOI: 10.1021/acs.inorgchem.8b00486
Inorg. Chem. XXXX, XXX, XXX−XXX

Table 3. Summary of Experimentally Deconvoluted MCD Bands of Complexes 1−4

	energy/sign							
band	1		2		3		4	
1	12500	−	10550	−	9850	−	14150	+
2	13730	+	12390	+	12150	+	16070	+
3	17030	+	17580	+	17520	+	18060	−
4	23390	−	23800	+	23760	+	19400	−
5			25000	+			20650	+
6			28550	+			21810	−
7							23860	−
8							25600	+
9							26510	+
10							28920	−
11							30600	+
12							32360	−

Table 4. Summary of Experimentally Deconvoluted MCD Bands of Complexes 5−7.

	energy/sign								
band	5			6			7		
1	18090	−	*z*	13400	−	*z*	12910	+	*x*
2	19380	−	*z*	18980	+	*z*	18446	+	*z*
3	21570	−	*z*	20340	+	*z*	21510	−	*z*
4	25050	+	*y*, *z*	24170	+	*z*	25050	−	*z*
5	26540	+		29690	−	*z*	26850	+	
6	28390	+		32600	−	*z*	28180	+	*z*
7	30650	−		35860	+	*z*	30150	+	*z*
8	32760	−					31840	−	*y*
9							33290	+	

17600 cm^{-1} for all three complexes. All bands exhibit strong temperature dependence (Figure D5), indicating that these signals arise through a *C*-term mechanism. In all three complexes, a somewhat poorly resolved vibrational progression is present in both the first and second bands, both of which may be fit with the same frequency. A frequency of 695 cm^{-1} was used in the case of **1** and 680 cm^{-1} for **2** and **3**. On this basis, it is likely that these features compose a pseudo-*A*-term signal, which arises from the overlap of two related *C* terms. Several additional features arise at energies above 20000 cm^{-1} in all three complexes. For **1**, a broad negative band around approximately 23400 cm^{-1} is seen. In **2**, the energy range is somewhat better resolved, and several additional positive features appear at 23800 and 25000 cm^{-1}. Last, an additional positive feature may be resolved in **3** at 23760 cm^{-1}. Unfortunately, because of low intensity and significant issues in achieving reasonable S/N ratios, the energy ranges of the MCD spectra for complexes **1**−**3** remain relatively limited, particularly for the solid-state spectra acquired for complexes **1** and **3**.

5.3.1.2. Compound 4. In the nonoxo "bare" V(IV) complex **4**, the spectrum appears drastically different from those of complexes **1**−**3** (Figure 4). All bands exhibit direct temperature and field dependence and are therefore assigned as features arising through a *C*-term mechanism. Both the UV−vis absorption and MCD spectra are highly featured, allowing a reasonable correlation between the two to be made and making it possible to postulate which bands of the MCD form pseudo-*A* terms and which arise as independent *C* terms. This more detailed deconvolution, in conjunction with the absorption spectrum of **4**, is provided in Figure D6. The low-energy portion of the spectrum from 13000 to 17000 cm^{-1} shows a weak positive MCD signal while exhibiting an intense (ε = ~6000 M^{-1} cm^{-1}) feature in the absorption spectrum. This is followed by several distinguishable features at 18060 and 19400 cm^{-1} (bands 3 and 4), which exhibit reasonable intensity in both the absorption and MCD spectra. These are, in turn, followed by a negative pseudo-*A* term centered at 21100 cm^{-1}, which is formed by bands 5 and 6. Next, a broad feature centered at 24600 cm^{-1} in the absorption spectrum correlates with a positive pseudo-*A* term from the overlap of bands 7 and 8. Several additional features appear at higher energies (bands 9−12), although these appear fairly weak in the MCD relative to the absorption spectra.

5.3.2. V(III) Complexes. To date, only the diffuse-reflectance electronic absorption spectrum of **7** has been reported,[24] and discrepancies in the literature on the assignments and analysis of electronic absorption and MCD spectra of **5** and **6** merit additional investigations.[22,68,69] These data are also particularly critical to formulating objective comparisons with theory, which will be presented later. The band-fit MCD spectra of complexes **5**−**7** are presented in Figure 5. Deconvolutions of these spectra were performed in a manner identical with those described above for compounds **1**−**4**, in which a minimum number of bands with consistent energies and bandwidths were optimized for all temperatures and fields measured, allowing only the

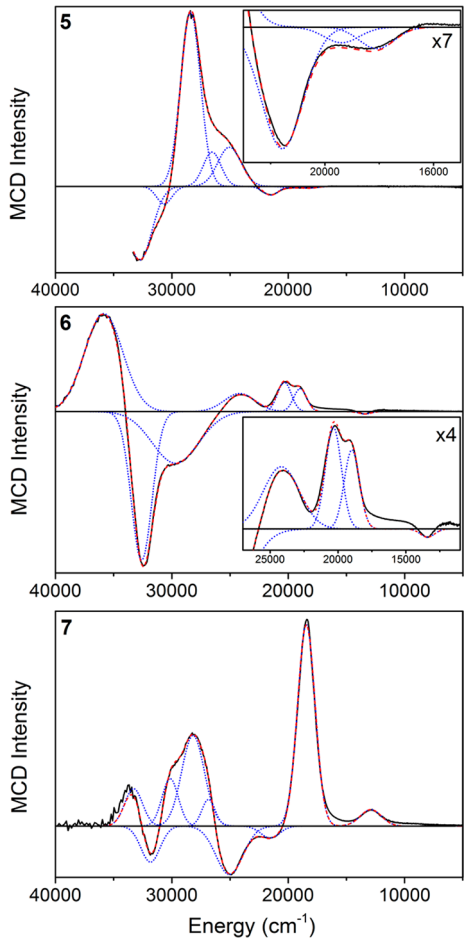

Figure 5. Band-deconvoluted 5 K and 5 T MCD spectra of (top) **5**, (middle) **6**, and (bottom) **7**. All spectra were obtained as finely ground powders pressed in KBr.

DOI: 10.1021/acs.inorgchem.8b00486
Inorg. Chem. XXXX, XXX, XXX−XXX

intensity to vary. A summary of fit bands for complexes **5**–**7** is provided in Table 4 and the temperature-dependent series in Figure D7. Additionally, the UV–vis absorption spectra are provided in Figure D8.

*5.3.2.1. Compound **5**.* Complex **5** presents a rich MCD spectrum containing both relatively weak and intense features (Figure 5), all of which exhibit strong temperature and field dependencies and therefore likely arise through a *C*-term mechanism. The spectrum is dominated by a large positive feature around 28000 cm^{-1} and its lower-energy shoulder, which together may be fit by three bands centered at 25050, 26540, and 28390 cm^{-1}. These are followed by several negative features centered at 30650 and 32760 cm^{-1}. Lower in energy, two weak negative features centered around 18500 and 21500 cm^{-1} arise. The unusual broadness of the first feature at 18500 cm^{-1} requires two Gaussian bands centered at 18090 and 19380 cm^{-1} for an adequate fit to be obtained, while the second may be simulated with a single Gaussian centered at 21570 cm^{-1}. The slight positive signal seen around 16000 cm^{-1} does not exhibit any significant temperature or field dependence and likely arises from background scattering.

Optical measurements of **5** have been reported by several groups, most recently by Krzystek and co-workers, who presented the temperature-dependent MCD spectrum up to 32000 cm^{-1}.[22] However, the spectra presented in their work was performed using a mulled sample with an unknown ratio of the α- and β- crystalline forms, while the present study utilizes the pure α form. Differences between the present spectrum and that of Krzystek and co-workers are discussed in greater detail in the Supporting Information. Generally, trivalent $M^{III}(acac)_3$ complexes commonly exhibit solvent- and temperature-dependent crystalline polymorphism, which can lead to discrepant results between several groups or even between several preparations of the same compound.[70,71]

*5.3.2.2. Compound **6**.* Similar to **5**, optical measurements of **6** have also been reported by Krzystek and co-workers, who have presented the temperature-dependent MCD spectrum up to 26000 cm^{-1}.[22] The spectrum presented in Figure 5 resolves the MCD of **6** from 5000 to 40000 cm^{-1}. All features across the spectrum exhibit a strong temperature dependence and thus must arise through a *C*-term mechanism. Similar to the previously reported spectrum, a low, sloping baseline of increasing intensity is present across the low-energy range of the spectrum. This baseline is first interrupted by a negative feature centered at 13400 cm^{-1}; while a very small increase above the baseline is seen around 12000 cm^{-1}, this cannot be fit objectively as a unique feature without additional experimental corroboration. This is again followed by a mild, sloping increase in the intensity, leading to two positive features centered at 18980 and 20340 cm^{-1}. The remaining spectrum is composed of a series of four very broad features. Three of these are so broad that the standard fitting procedure applied thus far, in which a maximum bandwidth is restricted to no greater than ~2 times the minimum bandwidth, would require the use of numerous bands. However, applying such an approach to these features would supply no additional useful information because they do not contain any clear additional inflection points. The first broad, positive feature is centered at 23900 cm^{-1}, which overlaps with a second, intense negative band centered at ~29700 cm^{-1} to form a negative pseudo-*A* term with an isosbestic point at 25840 cm^{-1}. At lower temperatures, the negative component appears as a shoulder to a sharper, even more intense band centered at 32560 cm^{-1}, while at higher temperatures, it forms its own distinguishable maximum (Figure D7). The intense, narrower negative feature at 32560 cm^{-1}, in turn, overlaps with a strong positive feature fit by a band centered at 35860 cm^{-1} to form a second pseudo-*A* term with an isosbestic point at 34000 cm^{-1}.

*5.3.2.3. Compound **7**.* While the major absorption features of **7** via diffuse reflectance were originally reported by Davies et al.,[24] the absorption spectrum of this compound is absent in the literature. The UV–vis/NIR spectrum (Figure D8) presents a weak, broad absorption peak centered at 12900 cm^{-1}, followed by a larger and somewhat sharper feature at 18500 cm^{-1}. The last easily discernible peak appears at 27250 cm^{-1} before rising into a more intense series of high-energy features starting at 37000 cm^{-1}. In the MCD (Figure 5), the feature at 12900 cm^{-1} may be adequately fit using either a single, broader Gaussian band or two smaller Gaussian bands centered at 12500 and 13250 cm^{-1}. Similar to **6**, **7** shows a continuous positive sloping background across the entire low-energy range of the spectrum; this has also been seen for $VBr_3(thf)_3$.[22] Next, the large positive peak centered at 18400 cm^{-1} is easily fit using a single Gaussian band. This is followed by several negative peaks centered at 21510 and 25050 cm^{-1}. The following positive feature appears as a convolution of three bands, with the dominant contribution centered at 28180 cm^{-1} and shoulders at 26850 and 30150 cm^{-1}.

5.4. VTVH-MCD. VTVH-MCD was collected for the three V(III) complexes in order to determine the polarizations of the observed electronic transitions, as well as to gain additional insight into the ground-state electronic properties of these molecules. Because of the large parameter space available during fitting (D, E/D, $g_{x,y,z}$, $M_{xz,yz,xy}$, and A_{sat}), modeling of the observed isotherms was restricted such that $g_x = g_y = g_z$, and D, E/D, and $g_{av.}$ were initially fixed to the values determined by SQUID in order to fit $M_{xz,yz,xy}$ and A_{sat}. Following initial fitting of $M_{xz,yz,xy}$ and A_{sat}, values of D, E/D, and g_{av} were allowed to vary.

VTVH-MCD measurements were performed at 18450, 21460, and 23810 cm^{-1} for **5** (Figure D9), 13370, 15380, 19120, 20240, 24100, 28570, and 32360 cm^{-1} for **6** (Figure D10), and 12900, 18240, 21550, 25000, 28250, 29940, and 31950 cm^{-1} for **7** (Figure D11). The initial modeling of **5** was performed starting from the spin-Hamiltonian parameters determined from the present SQUID study, as well as from previously reported HFEPR measurements.[22] Analysis of the global-fit error surfaces from either approach support an intermediate rhombicity (E/D = 0.14) with g_{av} = 1.75 and D = 7.1 cm^{-1}. The first three bands appear strictly *z*-polarized, while band 4 is a convolution of 42% *y*-polarized and 53% *z*-polarized. In complex **6**, simultaneous fitting of the spin-Hamiltonian and band polarizations for all bands supports a highly rhombic ground state (E/D = 0.33) with a relatively large ZFS ($|D|$ = 10 cm^{-1}) and g_{av} = 1.85. Interestingly, while fitting of the susceptibility and magnetization data of **6** did not show a particularly strong preference to D = 10 cm^{-1} versus D = 14 cm^{-1}, the VTVH-MCD isotherms cannot be reasonable fit using $|D| > 10$ cm^{-1}, thus supporting the smaller value. All bands are predominately *z*-polarized, although there is considerable mixing (15–30% *x*, *y* contribution). Finally, in complex **7**, analysis of the global-fit error surfaces support a small rhombicity (E/D = 0) with g_{av} = 1.8. Simulations for measurements at 29940 and 31950 cm^{-1} were bettered considerably when D was allowed to vary up to 9.6 cm^{-1}, although this only resulted in nominal improvements for

DOI: 10.1021/acs.inorgchem.8b00486
Inorg. Chem. XXXX, XXX, XXX–XXX

Table 5. Energies and Signs of the First Four SA-CASSCF(9,9)/NEVPT2-Calculated Excited States of Models 1a−3b and 4

	CASSCF(9,9)/NEVPT2 energy/sign									
state	1a		1b		3a		3b		4	
1	14490	−	15580	−	15140	−	16180	+	1010	+
2	15250	+	16370	+	15930	+	16990	+	3860	−
3	18240	+	17850	+	18120	+	17740	−	20440	−
4	31510	−	33100	+	37380	+	38770	−	24510	+

simulations of measurements at other energies. The most noticeable feature of any fit is that all observed VTVH-MCD follows single, pure polarizations; this implies that while the ground state contains very low rhombicity, the measured excited states are considerably rhombic in nature.

5.5. Theoretical Calculations. *5.5.1. MCD and Spin-Hamiltonian Calculations of V(IV) Complexes. 5.5.1.1. Calculations of the VO^{2+} Model Complexes (**1a**, **1b**, **3a**, and **3b**).* The SOC-CASSCF(9,9)/NEVPT2-calculated spin-Hamiltonian parameters of models **1a**−**3b** are provided in Table 2. The well-isolated $S = {}^1/_2$ ground states of models **1a**−**3b** all consist of a single unpaired electron that occupies a predominately V d_{xy}-centered orbital. As expected, coordination of Py or shortening of the V═O bond, which produces minor increases in g_x and g_y, is found because of the increased interaction along the z axis, while g_z remains, for the most part, invariant.

The calculated energies, MCD signs, and state assignments under C_{4v} symmetry for the first four ligand-field excited states of **1a**, **1b**, **3a**, and **3b** are presented in Table 5 and Figure 6, and

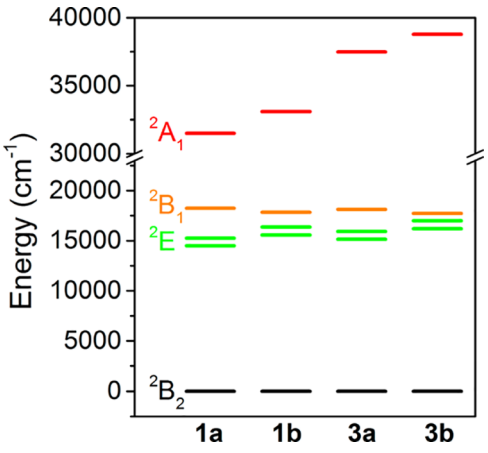

Figure 6. SA-CASSCF(9,9)/NEVPT2-calculated excitation energies for the first five states of model complexes **1a**−**3b**.

the calculated spectra in Figure D12. The first two excited electronic states involve excitations of the single unpaired electron from $b_2(d_{xy}) \rightarrow e(d_{xz},d_{yz})$ to generate the degenerate ^2E state. The third excited state ($^2B_1$) arises from the $b_2(d_{xy}) \rightarrow b_1(d_{x^2-y^2})$ and the final $^2A_1$ from the $b_2(d_{xy}) \rightarrow a_1(d_{z^2})$.

In this system, the Py ligand acts primarily as a σ donor through the two unpaired electrons present on nitrogen (Figure D13). This is clear upon comparison of the state energies of **3a**/**1a** or **3b**/**1b**. In both cases, the energy of $^2A_1$ increases greatly (5700−6000 cm^{-1}), while the ^2E state increases by a mere ∼600−650 cm^{-1}, implying that π interaction of Py with either V d_{xz} or d_{yz} is only a minor perturbation. Meanwhile, a comparison of **3a** with **3b** or **1a** with **1b** reveals that shortening of the V═O bond significantly impacts the ^2E and $^2A_1$ states, where ^2E increases by ∼1040−1060 cm^{-1} and $^2A_1$ by ∼1300−1570 cm^{-1}. Here, $^2B_1$ decreases by ∼380 cm^{-1}. Taking these two sets of comparisons into consideration, one can now pose the question of how these effects combine for a final outcome. Considering that the ligation of Py to $VO(acac)_2$ results in a trans effect that weakens the V═O bond, something already known from the observed V═O stretching frequencies reported in previous IR studies,[27] it is fairest to draw our comparisons between **3a** and **1b**. With both coordination of Py and a lengthening of the V═O bond by 0.03 Å, it is seen that the energy of the ^2E state *decreases* by ∼440 cm^{-1}, while that of $^2A_1$ *increases* by ∼4400 cm^{-1}. Additionally, $^2B_1$ is nearly invariant, increasing by only 270 cm^{-1}.

With these correlations in hand, we may return to the task of interpreting the observed spectra of **1**−**3**. As was just shown, our calculations predict a drop in the energy of the ^2E state upon coordination of an additional axial substituent and subsequent weakening of the V═O bond; similarly, we have seen that the energies of bands 1 and 2 are decreased in complexes **2** and **3**, relative to complex **1** (Figure 6). Therefore, we assign bands 1 and 2 to the ^2E state. Additionally, the relatively energy-invariant band 3 is assigned to the $^2B_1$ state. Meanwhile, our calculations predict the $^2A_1$ state to be considerably higher in energy, well outside of the observed range and unfortunately preventing the assignment of this state for **1**−**3** in the present study. However, the ligand-field transition energies of $VO(acac)_2$ have recently been reported by resonant inelastic X-ray scattering (RIXS) studies of $VO(acac)_2$. These reported values are in good agreement with those observed presently, and an additional higher-lying state around ∼26000 cm^{-1} has been observed and assigned to $^2B_2 \rightarrow {}^2A_1$.[72] With this estimate of the $^2A_1$ state, our current calculation overestimates this transition by ∼5000 cm^{-1}, which is still not unreasonable for the employed method.

To further support our assignments, we can individually determine the signs of the two $^2B_2 \rightarrow {}^2E$ transitions, which give rise to the pseudo-A term formed by bands 1 and 2 in complexes **1**−**3**. This term arises predominately through SOC between the $^2E_y(d_{xy}\rightarrow d_{yz})$ and $^2E_x(d_{xy}\rightarrow d_{xz})$ states; because of the asymmetry imposed by the $acac^-$ ligand in **1** and **2** (as well as by Py in **3**), $^2E_y(d_{xy}\rightarrow d_{yz}) < {}^2E_x(d_{xy}\rightarrow d_{xz})$. As d−d transitions are parity-forbidden, the transition dipole moments of the $^2B_2 \rightarrow {}^2E$ excitations must arise through overlap of the metal-centered d orbitals with the ligand O p orbitals. In general, the MCD C-term parameter C_0 for an $S = {}^1/_2$ system between the $2S + 1$ (with S being the total spin of the state) components of the spatially nondegenerate ground state A, the spatially nondegenerate excited J set of states, and the intermediate K set of states, in the presence of SOC, is described by the following equation:[31]

DOI: 10.1021/acs.inorgchem.8b00486
Inorg. Chem. XXXX, XXX, XXX−XXX

$$C_0 = -\frac{1}{6}\sum_{xyz}\epsilon_{xyz}g_z\sum_{K\neq A,J}\{\Delta_{KJ}{}^{-1}D_x^{AK}D_y^{AJ}L_z^{KJ}\} + \{\Delta_{KJ}{}^{-1}D_x^{AJ}D_y^{AK}L_z^{AK}\} \quad (5)$$

where D_i^{IJ} describes the Cartesian component ($i = x, y,$ or z) of the effective transition dipole moment between states I and J, $\Delta_{IJ}{}^{-1}$ is their energy difference, and ϵ is the Levi−Civitta symbol.

Focusing on the lower energy transition, we will assign $A = {}^2B_2(d_{xy})$ and $J = {}^2E_y(d_{xy}\rightarrow d_{yz})$. To simplify this equation, first all other excited states besides ${}^2E_x(d_{xy}\rightarrow d_{yz}) = A \rightarrow K$ are neglected. Rotating d_{yz} counterclockwise into d_{xz} leads to a positive overlap, and thus $L_z^{KJ} > 0$. Additionally, we approximate that $D_x^{AJ} \ll D_x^{AK}$ and $D_y^{AK} \ll D_y^{AJ}$, allowing us to reduce eq 5 to

$$C_0 = -\frac{1}{6}\sum_{xyz}\epsilon_{xyz}g_z\left\{\frac{L_z^{KJ}}{\Delta_{KJ}}D_x^{AK}D_y^{AJ}\right\} \quad (6)$$

This allows the sign of the resulting MCD C term at the saturation limit to be evaluated following

$$C_0(E_y) \propto -\langle S_z\rangle\frac{L_z^{KJ}}{\Delta_{KJ}}(D_x^{AK})(D_y^{AJ}) < 0 \quad (7)$$

when $\Delta_{KJ} = E_K - E_J > 0$. From the calculated transition dipole moments, it then follows that positive Δ_{KJ} results in the absorption of right-handed photons, producing a negative MCD signal. Meanwhile, if we assign the higher energy E_x transition as $A \rightarrow J$ and E_y as $A \rightarrow K$, a positive sign will result as $\Delta_{KJ} = E_K - E_J < 0$. Together, the transitions $E(d_{xy}\rightarrow d_{xz,yz})$ form a positive pseudo-A term, which corresponds well with the MCD bands 1 and 2 observed for complexes **1**−**3**.

5.5.1.2. Calculations of the $VCl_2(acac)_2$ Complex (4). Unlike the vanadyl series, **4** lacks the strong axial oxo bond that dominates the electronic structure of complexes **1**−**3**. Instead, the softer binding Cl^- ligands result in a mild axial elongation and approximate D_{4h} symmetry. Under this assumption, the ground state would be characterized as ${}^2E_g$ arising from the singly occupied $e_g(d_{yz},d_{xz})$, and the relative energetic ordering of the d manifold of **4** follows an $e_g(d_{yz},d_{xz}) < b_{2g}(d_{xy}) \ll a_{1g}(d_{z^2}) < b_{1g}(d_{x^2-y^2})$ motif. In reality, as evidenced from EPR (Figure 3a) and in our calculations, the ${}^2E_g$ ground state is split significantly. Indeed, the relative energies of the ligand-field orbitals from our calculations predict $d_{yz} < d_{xy} < d_{xz} \ll d_{z^2} < d_{x^2-y^2}$, implying that π interactions between $acac^-$ and V(IV) are significant. Therefore, we will proceed with our discussion of the excited states using D_{2h} symmetry labeling from here forward.

Under D_{2h} symmetry, the ${}^2B_{3g}$ ground state arises predominately from the singly occupied V d_{yz}, and the relative energetic ordering of the d manifold of **4** follows a $b_{3g}(d_{yz}) < b_{1g}(d_{xy}) < b_{2g}(d_{xz}) \ll 1a_g(d_{z^2}) < 2a_g(d_{x^2-y^2})$ motif. Similar to the $VO(acac)_2$ series, the ligand-field excited states arise from a series of one-electron excitations, starting with the ${}^2B_{1g}$ originating from the $b_{3g}(d_{yz}) \rightarrow b_{1g}(d_{xy})$ transition (state 1 of Table 5). Slightly higher in energy, $b_{3g}(d_{yz}) \rightarrow b_{2g}(d_{xz})$ generates the ${}^2B_{2g}$ state, while $b_{3g}(d_{yz}) \rightarrow 1a_g(d_{z^2})$ and $2a_g(d_{x^2-y^2})$ comprise the 1-${}^2A_g$ and 2-${}^2A_g$, respectively. The SOC-CASSCF(9,9)/NEVPT2 magnetic S = 1/2 ground state spin-Hamiltonian parameters present a rhombic ground state with $g_x = 1.928$, $g_y = 1.843$, and $g_z = 1.736$. This is a significant underestimation of the experimentally determined $g_x = 1.984$, $g_y = 1.943$, and $g_z = 1.807$, particularly in terms of g_z, likely due to an overestimation of the calculated 1-${}^2A_g$ and 2-${}^2A_g$ states.

The calculated SA-CASSCF(9,9)/NEVPT2 excited states of **4** presented in Table 5 (with spectra provided in Figure D14) imply that only the 1-${}^2A_g$ (20440 cm^{-1}) and 2-${}^2A_g$ (24510 cm^{-1}) states may be assigned within the observed experimental range. The overlap of these two terms forms a pseudo-A term with a predominately negative component. Experimentally, the C/D ratios of bands 3−6 (Table D1) all lie within a reasonable range (0.03−0.04) for a ligand-field-type assignment. Additionally, an even higher C/D ratio is found for band 9 (0.06), but the extinction coefficient of this band is also considerably higher (~6130 M^{-1} cm^{-1}) and therefore unlikely to be ligand-field-centered. These high ratios are due to the considerable SOC induced by Cl ($\zeta = -587$ cm^{-1}), allowing charge-transfer (CT)-type transitions between V(IV) and Cl^- to gain considerable intensity in the MCD and therefore making a clear assignment of the ligand-field transitions difficult. On the basis of the calculated sign and relative energy splitting, we assign the experimental bands 4 and 5 of **4** in Table 5 to the 1-${}^2A_g$ and 2-${}^2A_g$ states.

Table 6. Energies and Signs of the First 10 SA-CASSCF(12,10)/NEVPT2-Calculated Triplet States of Complexes 5−7

	CASSCF(12,10)/NEVPT2 energy/sign					
eigenstate	5		6		7	
${}^3T_1$	6.42	+	10.81	−	6.35	+
	810	+	892	+	1191	+
	961	+	1305	−	1390	+
${}^3T_2$	18574	−	13374	+	12494	+
	18909	−	13534	−	12669	+
	19109	+	14244	−	13080	+
${}^3T_1$	26149	−	21094	+	19493	+
	26768	+	21598	+	19690	+
	27788	−	23111	+	20153	+
${}^3A_2$	38122	+	28004	+	25747	+

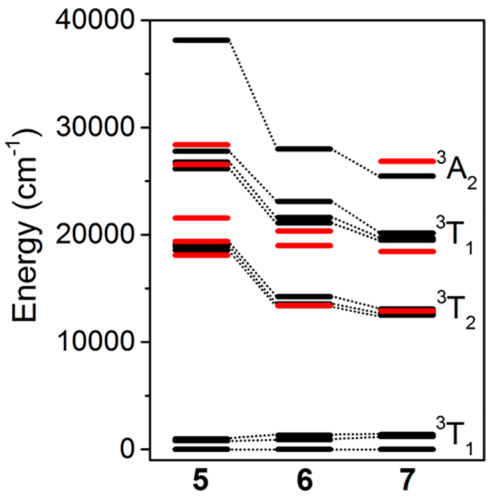

Figure 7. Comparison of the SA-CASSCF(12,10)/NEVPT2-calculated triplet states of **5**−**7** with ligand-field state assigments (black) alongside the experimentally assigned states (red).

DOI: 10.1021/acs.inorgchem.8b00486
Inorg. Chem. XXXX, XXX, XXX−XXX

5.5.2. MCD and Spin-Hamiltonian Calculations of V(III) Complexes. The state-averaged (SA)-CASSCF(12,10)/NEVPT2-calculated triplet-state energies of complexes **5**−**7** are presented in Table 6 and Figure 7, while the corresponding spectra are provided in Figure D15. The first 10 triplet and 15 singlet roots were calculated for **5**−**7**.

*5.5.2.1. Calculations of the V(acac)$_3$ Complex (**5**).* The SOC-CASSCF(12,10)/NEVPT2-calculated ground state of **5** is comprised of the nondegenerate $^3A_2$ state. Here, the calculated spin-Hamiltonian parameters (Table 1) describe the ground state as near-axial (E/D = 0.06, $g_\perp$ = 1.747 and 1.729, and $g_\parallel$ = 1.937), with a ZFS of D = 9.6 cm^{-1}.

The calculated ground state of **5** consists of a near-axially split 1-$^3T_1$ term to form $^3A_2$ and ^3E, with $^3A_2(T_{1g})$ < $^3E(T_{1g})$ split by 880 cm^{-1} and $^3E(T_{1g})$ further split by 150 cm^{-1}, with all transitions resulting in positive MCD signs (Table 6). The first excited state ($^3T_2$) is calculated to be only very mildly split (400 cm^{-1}), and similar to the ground state, $^3A_1(T_{2g})$ < $^3E(T_{2g})$. Here, $^3E(T_{2g})$ is split by 200 cm^{-1}. Together, these form a (−, −, +) motif in terms of the MCD sign, with the combined negative components having about 4 times greater intensity than the positive. The energetic proximity of the observed bands 1−3 (all negative) to these calculated transitions suggests that they also belong to $^3T_{2g}$; while no positive feature is observed, this may be masked by the strong, positive band 4. Moving forward, the calculated 2-$^3T_1$ forms a negative feature split as $^3E(2\text{-}^3T_{1g})$ < $^3A_1(2\text{-}^3T_{1g})$ by 1330 cm^{-1}, with $^3E(2\text{-}^3T_{1g})$ further split by 620 cm^{-1}. This transition appears with an intensity ∼18 times greater than that of $^3T_2$. In this energetic region, experimental bands 5 and 6, which are split by 1900 cm^{-1}, present two very large positive features. It is notable that the absolute intensity of band 6 is ∼20 times greater than that of band 4, which we have assigned as part of $^3T_2$. Therefore, based on the good agreement between the experimental and calculated energies and relative intensities, bands 5 and 6 are assigned to 2-$^3T_1$. This assignment is also in excellent agreement with recent RIXS studies of complex **5**, which have assigned 2-$^3T_1$ to two transitions around ∼27400 and ∼29800 cm^{-1}, respectively.[72] Discrepancies between the calculated and experimental signs may arise through the coupling of 2-$^3T_1$ with a neighboring CT states; since CT states are not accounted for in the present calculation, such effects are not presently taken into account. At present, we have not taken this into consideration because doing so often requires forbiddingly large active spaces to fully and accurately describe the CT states.

*5.5.2.2. Calculations of the VCl$_3$(thf)$_3$ Complex (**6**).* The SOC-CASSCF(12,10)/NEVPT2-calculated ground state of **6** is considerably rhombic (E/D = 0.18), with a large ZFS of D = 16.2 cm^{-1}. Values of $g_\perp$ = 1.594 and 1.689 and $g_\parallel$ = 1.946 (g_{av} = 1.743) were obtained, in reasonable agreement with what we have seen thus far experimentally (Table 1; g_{av} = 1.72).

While truly meridonal in geometry, the calculated triplet states of **6** appear to follow a *pseudo*trigonal distortion, in which each ^3T is split into ^3E + ^3A states, similar to the case of **5**. Because of this behavior, it is useful to continue the use of this nomenclature for later comparisons of complexes **5**−**7**. The calculated ground-state 1-$^3T_1$ is split in a ^3A < ^3E fashion by 1100 cm^{-1}, with ^3E being further split by 400 cm^{-1}. The first calculated excited state, $^3T_2$, is split as ^3E < ^3A by 790 cm^{-1}, with ^3E further split by 160 cm^{-1}, resulting in a (+, −, −) motif in the MCD. Here, ^3E forms a negative pseudo-*A* term, which overlaps with the additional negative component from ^3A (Table 6). Here, the calculated energy of this negative feature is in excellent energetic agreement with the negatively signed band 1 of the experimental MCD and is therefore assigned in this manner. 2-$^3T_1$ is considerably more distorted, with ^3E < ^3A by 1770 cm^{-1} and ^3E further split by 500 cm^{-1}. Interestingly, all three components are calculated to generate a positive sign in the MCD; while overestimating by ∼2000−3000 cm^{-1}, which is still quite reasonable by CASSCF/NEVPT2, these excited states correspond well with the positive bands 2 and 3 of the experimental spectrum. Last, the $^3A_2$ transition is calculated to have a positive sign at 28000 cm^{-1}. While this may very well be present in some respect, the relatively low calculated intensity (compared to 2-$^3T_1$) and the presence of a large, broad negative feature in this region prevent us from ascertaining a precise experimental assignment of this transition.

*5.5.2.3. Calculations of the VCl$_3$ttcn Complex (**7**).* The SOC-CASSCF(12,10)/NEVPT2-calculated spin-Hamiltonian parameters of **7** produce a considerable axial splitting of D = 9.53 and a relatively low rhombicity of E/D = 0.057, both of which are somewhat overestimated compared to the experimentally determined values presented in Table 1. Meanwhile, the calculated *g*-tensor values of 1.921, 1.728, and 1.743 (g_{av} = 1.797) are in excellent agreement with the experiment [g_{av}(Magn.) = 1.77; g_{av}(VTVH-MCD) = 1.8]. The calculated triplet excited-state energies are presented in Table 6. Similar to **5**, the calculated MCD spectrum mirrors a distorted *pseudo*octahedral spectrum, forming three dominant positive features that correspond to the $^3T_2$, 2-$^3T_1$, and $^3A_2$ states (in order of increasing energy). As seen previously for both **5** and **6**, the splitting of the $^3T_2$ and $^3T_1$ terms follows a *pseudo*trigonal distortion, in which each ^3T term is split into the ^3A and ^3E states and ^3E is further split to a lesser degree. In the ground state, ^3A and ^3E of 1-$^3T_1$ are strongly split by 1290 cm^{-1}, with ^3A < ^3E, while both $^3T_2$ and 2-$^3T_1$ follow a ^3E < ^3A motif and are more mildly split, by 500 and 560 cm^{-1}, respectively. The ^3E states of 1-$^3T_1$, $^3T_2$, and 2-$^3T_1$ are further split by 200, 175, and 200 cm^{-1} each.

As noted before, all triplet excited states calculated for **7** result in a net positive MCD intensity. The calculated $^3T_2$ matches well with band 1 in terms of both energy and sign and is assigned thusly. Furthermore, the single large band 2 is assigned to 2-$^3T_1$ because of its excellent correlation with calculated values. Last, the small positive band 5 is assigned to $^3A_2$, again because of strong support in terms of the calculated energy, sign, and relative intensity.

5.5.3. Ligand-Field Treatment of Parameters. In this section, we interpret the ligand-field properties of complexes **1**−**7** from the experimental and calculated data above determined in a stepwise fashion through the AOM. In this well-established ansatz, the 3d-t_{2g}(d_{xy},d_{xz},d_{yz}) and e_g($d_{x^2-y^2}$,d_{z^2}) orbitals of metal complexes containing anionic ligands are destabilized through σ- and π-type interactions, giving rise to antibonding orbital energies of $3e_\sigma$ and $4e_\pi$, respectively. These are further perturbed by asymmetry, requiring the employed AOM model to be customized on a case-by-case basis. The formulations of these customized approaches are described below, while the resulting calculated ligand-field parameters are summarized in Table 7 for complexes **1**−**4** and in Table 8 for complexes **5**−**7**.

*5.5.3.1. VO^{2+} Complexes (**1**−**3**).* The AOM analysis protocol developed to extract the ligand-field parameters from the experimental data of complexes **1**−**3** and the computed data of

DOI: 10.1021/acs.inorgchem.8b00486
Inorg. Chem. XXXX, XXX, XXX−XXX

model complexes **1a**, **1b**, **3a**, and **3b** are presented in section C of the Supporting Information. In complexes **1**−**3**, bands 1 and 2 of Table 3 have been assigned in C_{4v} symmetry to the split ^2E state, while band 3 is assigned to $^2B_1$; as mentioned before, we unfortunately have not been able to conclusively assign the $^2A_1$ state of these complexes based upon our current observations. Therefore, our analysis is limited to the accurate determination of parameters e_π(O), $\Delta e_{\pi s}$(acac), and e_σ(acac) (Table 7). To provide estimates of 10Dq and e_σ(acac), placeholder values of the 2-$^2A_1$ state were used based upon previous RIXS studies of **1** and the relative shift seen between **1b** and **3a** in our CASSCF(9,9)/NEVPT2 calculations, employing 26000 cm^{-1} (for **1**) and 31000 cm^{-1} (**2** and **3**).[72] In **1**, this assignment results in values of e_σ(O) ≅ 20730 cm^{-1} and 10Dq ≅ 14080 cm^{-1}.

While the fourth ligand-field transition of complexes **1**−**3** cannot be conclusively assigned experimentally, this information is readily available from theory in models **1a**−**3b**. The ligand-field parameters presented in Table 7 were modeled by the assignment of excited states 1 and 2 to ^2E, 3 to $^2B_1$, and 4 to $^2A_1$, as previously mentioned.

Shortening of the V═O bond (comparing **1a**/**1b** or **3a**/**3b**) interestingly results in a relatively small *decrease* in 10Dq. This arises from the strong π interaction of the terminal oxo with vanadium; while both σ and π-oxo interactions strengthen with a shortened V═O distance, the π interaction increases at a greater rate, resulting in a decrease in 10Dq. Meanwhile, coordination of Py (comparing **1a**/**3a** or **1b**/**3b**) drastically increases 10Dq by ∼2400 cm^{-1}. This occurs predominately through the overall increased σ interaction, raising the energy of $^2A_1$ significantly. Meanwhile, coordination of Py only nominally increases the fit values of e_π(O) by 270 cm^{-1}, a significantly smaller effect than decreasing of the V═O coordinate.

5.5.3.2. Complex 4. We have just seen that the ligand fields of complexes **1**−**3** are dominated by the V═O interaction, with the $acac^-$ ligands acting as a relatively minor perturbation. In the case of complex **4**, on the other hand, the interaction of $acac^-$ with V(IV) becomes a more significant force. According to our calculations, the ^2E_g (in D_{4h}) ground state of **4** is split by ∼3800 cm^{-1} to form the $^2B_{3g}$ and $^2B_{2g}$ states (in D_{2h}), with $^2B_{3g}$ < $^2B_{2g}$. In a one-electron picture, the $^2B_{3g}$ ground state is predominately composed of a singly occupied V $3d_{yz}$-centered orbital. The energies of V d_{yz} and d_{xz} in **4** depend upon both the cylindrical e_π(Cl) and $e_{\pi s}$(acac)/$e_{\pi s'}$(acac) interactions, while the energy of V d_{xy} depends on $e_{\pi c}$(acac). As also employed for complexes **1**−**3**, we may introduce the parameter $\Delta e_{\pi s}$(acac) = $e_{\pi s}$(acac) − $e_{\pi s'}$(acac) to provide insight into the Orgel effect described above. However, our previous assumption that $e_{\pi c}$(acac) ≈ 0 is no longer valid, and it is not possible to deconvolute $e_{\pi c}$(acac), $e_{\pi s}$(acac), and e_π(Cl) without making further assumptions. We may then fit the system using the approximation that e_π(Cl) = 0; this is done based upon the relatively small (>3%) contribution of Cl^- to the unoccupied V $d_{xz,yz}$-dominated molecular orbitals. This allows us to at least determine a parameter that contains a convolution of $e_{\pi c}$(acac) and $e_{\pi s}$(acac), which provide a gauge of how much greater $e_{\pi c}$(acac) is than $e_{\pi s}$(acac). We will refer to this as $e_{\pi c}$*(acac). This leaves our model with two σ-based parameters [e_σ(Cl) and e_σ(acac)], as well as two π-based parameters [$\Delta e_{\pi s}$(acac) and $e_{\pi c}$*(acac)]. While all four parameters may be fit based on the SA-CASSCF(9,9)/NEVPT2-calculated excited states, only 1-^2A_g and 2-^2A_g are seen in experiment, limiting our ability to fit $\Delta e_{\pi s}$(acac) and $e_{\pi c}$*(acac). Upon a comparison of **4** with **1**−**3**, the e_σ(acac) interaction is increased somewhat as expected because of the movement of vanadium into the $acac^-$ plane (Table 7).

5.5.3.3. Complex 5. The deceptively simple complex **5** has a considerable history of previous ligand-field assignments, which contain numerous discrepancies. The first proposed assignment of the ligand field of **5** was made by Piper and Carlin,[69] who hypothesized that the features observed at 18200 and 21700 cm^{-1} arise from the $^3T_{1g} \rightarrow {}^3T_{2g}$, $^3T_{1g}$ transitions, respectively. The same assignment was later proposed by Machin and Murray,[68] who proposed B = 285 cm^{-1} [B = 860 cm^{-1} for the free V(III) ion] and 10Dq = 18900 cm^{-1} under the assumption of O_h symmetry using the equations of Griffith.[73] This abnormally small value of B led Gregson et al.[66] to reanalyze these data; while they propose that B = 600 cm^{-1} and 10Dq = 22250 cm^{-1} would be reasonable considering similar values for other V(III) complexes, their reassignment of the observed transitions at 18200 and 21700 cm^{-1} as $^3A_2[^3T_1] \rightarrow {}^3E[^3T_2]$ and $^3A_2[^3T_1]$, assuming a trigonal-field distortion, required B = 328 cm^{-1} and 10Dq = 18060 cm^{-1}. More recently, Krzystek et al.[22] offered a revision of these assignments on the basis of MCD. In their work, the transitions observed at 18200 and 21700 cm^{-1} were assigned to $^3A_2[^3T_1] \rightarrow {}^3A_1[^3T_2]$ and $^3E[^3T_2]$, while $^3A_2[^3T_1] \rightarrow {}^3A_1[^3T_1]$ and $^3E[^3T_1]$ were proposed to correspond to features observed at 27400 and 29700 cm^{-1}. With this new set of assignments, ligand-field parameters of B = 684 cm^{-1} and 10Dq ≈ 20000 cm^{-1} were proposed. This fit also requires a relatively large trigonal splitting of 2100 cm^{-1}, although this is not particularly unusual because the trigonal splitting of $V(H_2O)_6^{3+}$ has been reported to be as large as 1940 cm^{-1}.[74]

As noted previously, the in-plane ($e_{\pi c}$) and out-of-plane ($e_{\pi s}$) π interactions in ligands such as $acac^-$ are inequivalent. Additionally, as mentioned for the case of complexes **1**−**3**, the extended out-of-place π-electron network of $acac^-$ leads to phase relations of the out-of-plane ligand orbitals, forming symmetric (ψ, in-phase) and antisymmetric (χ, out-of-phase) sets as described by Orgel[75] and elaborated by Ceulemans et al.[76] (see Scheme C1). This further requires the out-of-plane π interaction $e_{\pi s}$ to be described as an average of the in-phase $e_{\pi s}(\psi)$ and out-of-phase $e_{\pi s'}(\chi)$.

A model coordinate system of **5** described in terms of the polar angle θ, twist angle ϕ, bite angle α, and dihedral angle ψ (Scheme 2) was generated by averaging these angles in the core geometry of the observed crystal structure to generate a trigonal model with effective D_3 symmetry, where θ = 54.43°, ϕ = 60°, α = 88°, and ψ = 43.5°. When this model was applied, the following experimental assignments were made: $^3A_2(^3T_{1g}) \rightarrow {}^3E(T_{2g})$ to the average of 18090 and 19380 cm^{-1}, $^3A_2(^3T_{1g}) \rightarrow {}^3A_1(T_{2g})$ to 21570 cm^{-1}, $^3A_2(^3T_{1g}) \rightarrow {}^3E(T_{1g})$ to 26540 cm^{-1}, and $^3A_2(^3T_{1g}) \rightarrow {}^3A_1(T_{2g})$ to 28390 cm^{-1}. Because of the limited number of observables, $e_{\pi c}$ was fixed to two-thirds that of $e_{\pi s}$. Using the full matrix method, these assignments provided excellent fits (within ±60 cm^{-1} for transitions to $^3T_{2g}$ and ±180 cm^{-1} for transitions to $^3T_{1g}$) with the use of B = 519 cm^{-1}, 10Dq = 19730 cm^{-1}, e_σ = 8280 cm^{-1}, $e_{\pi s}$ = 1532 cm^{-1}, and $e_{\pi c}$ = 1021 cm^{-1}. The significantly large values of e_σ and e_π, combined with a small B, imply a considerable degree of covalency in the complex.

Similarly, an AOM fit was performed for the SA-CASSCF-(12,10)/NEVPT2-calculated excited states of **5**. Using a model identical with that implemented for the experimental

DOI: 10.1021/acs.inorgchem.8b00486
Inorg. Chem. XXXX, XXX, XXX−XXX

Table 7. Summary of Fit AOM Parameters for Complexes 1−4[a]

		ligand-field parameters				
complex		10Dq	e_σ(O)	e_π(O)	e_σ(acac)	$\Delta e_{\pi s}$(acac)
1	exp.	17090[c]	26730	11690	6000	740
1a[b]	C(9,9)/N	16450	25950	13620	6420	413
1b[b]	C(9,9)/N	16280	27660	14730	6280	433

		ligand-field parameters				
complex		10Dq	e_σ(O,N)	e_π(O,N)	e_σ(acac)	$\Delta e_{\pi s}$(acac)
2	exp.	20920[d]	15740	4870	6210	1120

		ligand-field parameters					
complex		10Dq	e_σ(O,N)	e_π(O)	e_σ(acac)	$\Delta e_{\pi s}$(acac)	e_π(N)
3	exp.	21130[d]	15720	8830	6200	1410	460
3a[b]	C(9,9)/N	18920	15980	13910	6370	413	770
3b[b]	C(9,9)/N	18640	16680	14980	6240	433	730

		ligand-field parameters				
complex		10Dq	e_σ(Cl)	$e_{\pi c}$(acac)[c]	e_σ(acac)	$\Delta e_{\pi s}$(acac)
4	exp.	20060	6240		6910	
	C(9,9)/N abbr.[e]	24940	7850		8550	
	C(9,9)/N	20950	6110	270	8200	1825

[a]The CASSCF(9,9)/NEVPT2 method is abbreviated as C(9,9)/N. [b]Derived using SA-CASSCF(9,9)/NEVPT2-calculated energies. [c]Supplemented using the RIXS-assigned 2-A_1 energy of **1** for fitting of the experiment at 10Dq.[72] [d]Supplemented with a 2-A_1-calculated energy shift in conjunction with the RIXS-assigned 2-A_1 energy of **1** for fitting of experimental at 10Dq.[72] [e]abbr. = "abbreviated" use of calculated roots to match those observed experimentally.

parameters, the calculated triplet electronic states were assigned as follows: $^3A_2(^3T_{1g}) \rightarrow {}^3E(T_{2g})$ to the average of 18574 and 18909 cm^{-1}, $^3A_2(^3T_{1g}) \rightarrow {}^3A_1(T_{2g})$ to 19109 cm^{-1}, $^3A_2(^3T_{1g}) \rightarrow {}^3E(T_{1g})$ to the average of 26149 and 26786 cm^{-1}, and $^3A_2(^3T_{1g}) \rightarrow {}^3A_1(T_{2g})$ to 27778 cm^{-1}. The resulting best fit was accomplished using B = 632 cm^{-1}, 10Dq = 19627 cm^{-1}, e_σ = 7128 cm^{-1}, $e_{\pi s}$ = 528 cm^{-1}, and $e_{\pi c}$ = 352 cm^{-1}, which provided errors of ±240 cm^{-1} for transitions to $^3T_{2g}$ and ±330 cm^{-1} for transitions to $^3T_{1g}$. The significant increase in B along with the drastic decreases in e_σ and e_π arises from the failure of CASSCF/NEVPT2 to fully account for electron correlation, a well-known problem with the method.

5.5.3.4. Complex 6. For analysis[77] of the rhombic complex **6**, the lowered strict C_2 symmetry of the complex allows π contributions of the thf and Cl ligands to be differentiated. While the Cl^- ligands are treated cylindrically, in which $e_{\pi s} = e_{\pi c}$, this is not applicable for the thf ligands, which are capable of only the contribution from the out-of-plane $e_{\pi s}$. Therefore, we may initially define the ligand-field strength in terms of 10Dq = $3e_\sigma - 2e_\pi(Cl) - e_{\pi s}(thf)$. Furthermore, the thf ligands are twisted an average of 34.6° out of the equatorial plane, while the axial thf is twisted by 43.3° out of the axial plane containing the three Cl ligands. Using the C_2-symmetrized model, a reasonable fit was obtained in which e_σ = 5290 cm^{-1}, e_π(Cl) = 700 cm^{-1}, and $e_{\pi s}$(thf) = 450 cm^{-1} with errors of ±100−160 cm^{-1} and B = 465 cm^{-1} with an error of ±2 cm^{-1}. Additionally, the ligand field of **6** was calculated for the SA-CASSCF(12,10)/NEVPT2-calculated excited states. To equate our calculations with the experiment, excited states belonging to $^3T_2$ and 2-$^3T_1$ were averaged as necessary to match experimental resolution. A further fit utilizing all calculated triplet roots was also performed, as summarized in Table 8. While the calculations reasonably estimate 10Dq, it is clear that a large overestimation of B is implicit regardless of the number of roots employed in the AOM model. As mentioned in the case of **5**, this is an inherent problem that arises from a failure to completely account for the electron correlation energy.

5.5.3.5. Complex 7. The ligand field of complex **7** shares commonalities with both **5** and **6** because it contains an effective trigonal symmetry (approximately C_{3v}) and cylindrical π bonding from the three coordinating Cl ligands. Additionally, the sulfur atoms of the 1,4,7-trithiacyclononane ligand are restricted in their ability to interact with the V(III) center because they are thioethers rather than thiols. This means that only one of the two open lobes of sp^3-hybridized sulfur is capable of overlapping with the central metal and thus only undergoes a σ-donor interaction. Therefore, **7** must be described in terms of an averaged e_σ for the Cl and S constituents, while e_π arises solely from interactions with Cl. In turn, we will treat 10Dq = $3e_\sigma$(Cl/S) − $2e_\pi$(Cl). Following from the MCD of **7** shown in Figure 5, the single broad band found at 12910 cm^{-1} is assigned to the $^3A_2(^3T_{1g}) \rightarrow {}^3E(T_{2g})$ and $^3A_1(T_{2g})$ transitions. Similarly, the single band at 18450 cm^1 is attributed to the $^3A_2(^3T_{1g}) \rightarrow {}^3E(T_{1g})$ and $^3A_2(T_{1g})$ transitions. Finally, the small feature at 26850 cm^{-1} is assigned as $^3A_2(^3T_{1g}) \rightarrow {}^3A_2(A_{2g})$. With these assignments, good agreement was found using 10Dq = 13800 cm^{-1}, B = 423 cm^{-1}, e_σ = 5310 cm^{-1}, and e_π(Cl) = 1060 cm^{-1}. Deviations of the corresponding transitions predicted with these parameters are ∼±100 cm^{-1}.

Furthermore, ligand-field analysis of the SA-CASSCF-(12,10)/NEVPT2-calculated electronic states of **7** was performed. Here, the included states were averaged to imitate the experimental assignments. To do so, the three components of each of the $^3T_2$ and $^3T_1$ excited states provided in Table 6 were averaged and used in the ligand-field analysis, giving a total of three bands (at 12748, 19779, and 25747 cm^{-1}) available for the fitting process. Doing so resulted in a reasonable fit using 10Dq = 13470 cm^{-1}, B = 533 cm^{-1}, e_σ = 5180 cm^{-1}, and e_π = 1040 cm^{-1}; deviations in the corresponding transitions generated by this set of parameters are ∼±170 cm^{-1}.

DOI: 10.1021/acs.inorgchem.8b00486
Inorg. Chem. XXXX, XXX, XXX−XXX

Table 8. Summary of Experimental and Calculated Ligand-Field Parameters of Complexes 5−7[a]

		ligand-field parameters					
complex		10Dq	B	B/B_0	e_σ	$e_{\pi s}$	$e_{\pi c}$
5	exp.	19730	519	0.603	8280	1530	1110
	C(12,10)/N abbr.	19630	632	0.734	7130	530	350
	C(12,10)/N	19480	638	0.741	7130	580	380
	C(2,5)/N	18540	829	0.963			
		ligand-field parameters					
complex		10Dq	B	B/B_0	e_σ	e_π(Cl)	e_π^s(thf)
6	exp.	14040	465	0.540	5210	700	450
	C(12,10)/N abbr.	14450	625	0.726	5620	910	590
	C(12,10)/N	14280	622	0.722	5780	1180	670
	C(2,5)/N	13490	865	1.004			
		ligand-field parameters					
complex		10Dq	B	B/B_0	e_σ	e_π(Cl)	
7	exp.	13800	423	0.491	5310	1060	
	C(12,10)/N abbr.	13470	553	0.642	5180	1040	
	C(12,10)/N	13500	560	0.650	5190	1040	
	C(2,5)/N	12630	826	0.959			

[a] B/B_0 calculated using the free-ion value of B = 861 cm^{-1} for V(III). The CASSCF(12,10)/NEVPT2 and CASSCF(2,5)/NEVPT2 methods are abbreviated as C(12,10)/N and C(2,5)/N, respectively. abbr. = "abbreviated" use of calculated roots to match those observed experimentally.

6. DISCUSSION

In the V(IV) series, we have investigated both common "vanadyl" and rarer nonoxo "bare" vanadium complexes. In the vanadyl series, the ligand field is dominated by the strong, covalent V═O interaction, which is responsible for determining the primary structure of the ligand-field manifold. Here, we have found that both our experiments and calculations support the general ligand-field scheme proposed by Ballhausen and Gray for the vanadyl hexaaqua ($[VO(H_2O)_5]^{2+}$) complex.[55] Despite the high covalency of the V═O bond, these complexes are quite sensitive to the sixth-ligand coordination. This is abundantly clear in both the experimental MCD spectra and calculated transition energies for models **1a**−**3b**. Upon a comparison of the MCD of complexes **1**−**3**, the low-energy pseudo-*A*-term feature is clearly dependent upon the axial coordination of the sixth ligand, shifting to increasingly lower energy when moving from **1** to **2** to **3**. The donor interactions of a variety of solvents with $VO(acac)_2$ have been reported previously by Linert and co-workers, who have shown through observation of the V═O stretching frequency that Py coordinates more strongly than acetonitrile.[27] Because one would anticipate that nPrCN and acetonitrile have similar donor properties, it is expected that nPrCN also coordinates more weakly to $VO(acac)_2$ than Py. This is most clearly manifested in the fact that $VO(acac)_2$Py may be precipitated and isolated, whereas $VO(acac)_2$nPrCN cannot. As the strength of the coordination is increased from uncoordinated in **1** to weakly coordinated in **2** to relatively strongly coordinated in **3**, the energetic position of the first pseudo-*A* term, assigned as ^2E, is decreased by approximately 1600 cm^{-1}. Interestingly, this effect is not as strongly reflected in the EPR spectra of these complexes. This is not particularly surprising; a σ-type axial perturbation will likely have the greatest effect on the energy of the V d_{z^2} orbital, which, according to the rotational relationships described above in eq 4, will not have a direct influence on the resulting *g*-tensor values. Furthermore, the ground states of the complexes are relatively well isolated (by at least 10000 cm^{-1}), and thus shifts in g_{eff} due to perturbations in the energies of excited ligand-field states will also be fairly small (0.01−0.02). At this limit, we approach the degree of error in our simulations, making clear trends difficult to formulate with EPR alone. The MCD, however, is a much more sensitive, and therefore more appropriate, method to observe these shifts because this technique directly probes the corresponding electronic excited states.

According to our calculations, we predict a significant increase in the energy of the $^2A_1$ state (by ∼4000 cm^{-1}) upon coordination of a sixth ligand, which accounts for the corresponding ∼2000 cm^{-1} increase in 10Dq. Unfortunately, the energy of the $^2B_2 \rightarrow {}^2A_1$ transition is predicted to be well outside of our current observable range because of the presence of a strongly absorbing feature (presumably of V═O ligand-to-metal CT character), and therefore this increase cannot be experimentally confirmed at present. Meanwhile, the $^2B_1$ state is calculated to be nearly invariant, while ^2E actually *decreases* in energy when accounting for the expected trans influence, which arises upon sixth-ligand coordination. Here, the calculated ^2E is predicted to produce a pseudo-*A* term, and the $^2B_1$ a single positive *C* term. Indeed, this matches well with what has been experimentally observed in MCD in terms of both sign and behavior, where the lowest-energy observed transitions shift to lower energy upon coordination, and a singly, slightly higher energy positive *C*-term appears to be nearly invariant. Therefore, the ^2E transition provides a promising gauge in determining the coordinative saturation of V(IV) vanadyl complexes. A comparison of the vanadyl series with the bare vanadium complex **4** further illustrates how the presence of a terminal oxo dominates the ligand field of the vanadyl complexes. While both **3** and **4** experience similar ligand-field splittings 10Dq, the ground state is now dominated by the single-electron occupation of V d_{yz}, and the predicted electronic structure is much closer to that of an octahedral complex.

In the V(III) series, considerable insight into the general electronic and magnetic properties of this ion in a distorted octahedral environment, including the trigonally distorted **5**, meridonal **6**, and facial **7**, has been gained by the combination of the determined spin-Hamiltonian parameters, electronic excited states, and corresponding calculations. Perhaps the

DOI: 10.1021/acs.inorgchem.8b00486
Inorg. Chem. XXXX, XXX, XXX−XXX

clearest trend among the V(III) complexes is the nephelauxetic effect (as diagnosed by B/B_0) observed as we move from 6O (harder) to 3Cl/3O to 3Cl/3SR_2 (softer) ligation. This is also reflected by the decrease in 10Dq across the series in a similar trend.

The observation of a positive ZFS D for both **5** and **7** (as well as for **6**, although the large rhombicity present in this complex prevents us from assigning an absolute sign) implies that the $^3T_1$ ground state is split such that $^3A < {}^3E$ in these complexes, counter to $^3E < {}^3A$ predicted by ligand-field theory for the geometries of these complexes; this is also supported by the observed MCD and our current calculations, as well as by previous high-field EPR measurements.[22] It is also particularly interesting to note that no ^3T term in either of the three complexes presents a clear pseudo-A term, as may be expected, with all assigned terms corresponding to a ^3T type transition showing a single sign in MCD. This behavior has also been observed for the $VBr_3(thf)_3$ complex,[22] and therefore this may present a characteristic of distorted octahedral V(III).

The state energies predicted by the SA-CASSCF(12,10)/NEVPT2 method for all three V(III) complexes are in excellent agreement with the experimentally observed transitions, well within the currently accepted error range for such calculations. Additionally, the spin-Hamiltonian parameters are reasonably well reproduced in terms of their sign and magnitude, implying again that the (12,10) active space utilized sufficiently captures the metal−ligand interactions in these complexes. It should be emphasized that employing a minimal (2,5) active-space calculation results in a large overestimation of the Racah parameter B (nearly the free-ion value), highlighting the importance of accounting for both the bonding and antibonding ligand-field orbital combinations in these complexes when utilizing a multiconfigurational method such as CASSCF. Our calculations also predict varying degrees of *pseudo*trigonal splitting in the ^3T states for all three complexes; while this is not surprising for **5** and **7**, it is interesting to observe for **6** because this complex does not contain a C_3 axis.

In accordance with the expectations from the ligand-field theory, we find that, by adding a single electron to the V(IV) ion, the system preferentially moves from an orbitally nondegenerate to a near-orbitally degenerate ground state. This is evidenced most clearly between the nonoxo **4** and all three of the presented V(III) complexes. From the presented spectroscopy, this is manifested for **4** in the Q-band EPR, where despite possessing effective D_{4h} symmetry, the complex undergoes a significant distortion to remove the degeneracy. This point is emphasized even further in our calculations, in which the splitting of the ^2E ground state is calculated to be 3860 cm^{-1}. Meanwhile, despite ligand-field theory predictions, the observed (VTVH-MCD and SQUID) and calculated positive ZFSs of all three V(III) complexes immediately indicate that all possess a near-orbitally degenerate $^3A_2$ ground state.

Finally, we have provided a summary of the most pertinent calculated and experimentally determined ligand-field parameters in Table 9.

Table 9. Summary of the Experimental and Calculated Ligand-Field Parameters of Complexes 1−7[a]

	experimental			calculated		
complex	10Dq	B	B/B_0	10Dq	B	B/B_0
1	17090[b]			16450[d], 16280[e]		
2	20920[c]					
3	21130[c]			18920[d], 18640[e]		
4	20060			20950		
5	19730	519	0.603	19480	638	0.741
6	14040	465	0.540	14280	622	0.722
7	13800	423	0.491	13500	560	0.650

[a]The presented calculated parameters are fit to the full set of ligand-field transitions as described in the text using the CASSCF(9,9)/NEVPT2 method for complexes **1**−**4** and the CASSCF(12,10)/NEVPT2 method for **5**−**7**. [b]Supplemented using RIXS-assigned 2-A_1 energy of **1** for fitting of the experiment 10Dq.[72] [c]Supplemented with a 2-A_1-calculated energy shift in conjunction with RIXS-assigned 2-A_1 energy of **1** for fitting of the experimental 10Dq.[72] [d]Calculated for models **1a** and **3a**. [e]Calculated for models **1b** and **3b**.

7. CONCLUSIONS

We have provided a detailed study of the magnetic and electronic properties of a series of V(IV) and V(III) complexes using a combination of complementing spectroscopic methods (magnetometry, EPR, and MCD) and high-level ab initio theory (SA-CASSCF/NEVPT2). Specifically, MCD has been utilized as an extremely information-rich technique that allows for both the unique assignment of ligand-field electronic transitions and discernment of the magnetic properties of paramagnetic systems. To this end, we have provided insight into the electronic and magnetic structures for a variety of molecular V(IV) and *pseudo*octahedral V(III) complexes. We have also shown that the SA-CASSCF/NEVPT2 method serves as a valuable tool for the accurate ab initio calculation of MCD of vanadium complexes.

As a further step, we have provided additional detailed insight into the electronic structures of these complexes through the development of a ligand-field analysis protocol based upon conventional AOM and ab initio ligand-field analysis. Through these methods, we have shown that the electronic properties of 5- and 6-coordinate V(IV) complexes depend significantly on the presence and type of sixth-coordination ligand, while the electronic properties of 6-coordinate V(III) complexes are quite sensitive to the σ- and π-donor abilities of the coordinating ligands.

Collectively, we hope that the combined experimental and computational analysis protocols presented here will aid in the characterization of vanadium in more complicated systems and the sagacious design of future vanadium-based complexes with the desired electronic and geometric properties. Further investigations are underway in our laboratories to apply the protocols presented here to challenging vanadium chemical systems in the fields of bioinorganic chemistry and heterogeneous catalysis.

■ ASSOCIATED CONTENT

Supporting Information

The Supporting Information is available free of charge on the ACS Publications website at DOI: 10.1021/acs.inorgchem.8b00486.

Sample preparation, a comparison of the present $V(acac)_3$ to the literature and between α- and β-$V(acac)_3$, details of the AOMX models, and supplementary figures, tables, and schemes (PDF)

Structural coordinates (ZIP)

DOI: 10.1021/acs.inorgchem.8b00486
Inorg. Chem. XXXX, XXX, XXX−XXX

AUTHOR INFORMATION

Corresponding Author

*E-mail: frank.neese@kofo.cec.mpg

ORCID

Casey Van Stappen: 0000-0002-1770-2231
Dimitrios Maganas: 0000-0002-1550-5162
Serena DeBeer: 0000-0002-5196-3400

Notes

The authors declare no competing financial interest.

ACKNOWLEDGMENTS

C.V.S., D.M., S.B., E.B., and F.N. thank the Max-Planck Society for funding and support. C.V.S. thanks the International Max-Planck Research School on Reactive Structure Analysis for Chemical Reactions (IMPRS-RECHARGE) for funding and Mihail Atanasov for his insightful discussions regarding ligand-field theory and assistance in utilizing the *AOMX* program. We also thank Dr. Claudi Weidenthaler and Jan Ternieden for their measurement of the powder X-ray diffraction pattern of $V(acac)_3$.

REFERENCES

(1) Weckhuysen, B. M.; Keller, D. E. Chemistry, spectroscopy and the role of supported vanadium oxides in heterogeneous catalysis. *Catal. Today* **2003**, *78* (1−4), 25−46.

(2) Rehder, D. The role of vanadium in biology. *Metallomics* **2015**, *7* (5), 730−42.

(3) Bignardi, G.; Cavani, F.; Cortelli, C.; De Lucia, T.; Pierelli, F.; Trifiro, F.; Mazzoni, G.; Fumagalli, C.; Monti, T. Influence of the oxidation state of vanadium on the reactivity of V/P/O, catalyst for the oxidation of n-pentane to maleic and phthalic anhydrides. *J. Mol. Catal. A: Chem.* **2006**, *244* (1−2), 244−251.

(4) Cavani, F.; Ligi, S.; Monti, T.; Pierelli, F.; Trifiro, F.; Albonetti, S.; Mazzoni, G. Relationship between structural/surface characteristics and reactivity in n-butane oxidation to maleic anhydride - The role of V^{3+} species. *Catal. Today* **2000**, *61* (1−4), 203−210.

(5) Centi, G.; Trifiro, F.; Ebner, J. R.; Franchetti, V. M. Mechanistic Aspects of Maleic-Anhydride Synthesis from C_4-Hydrocarbons over Phosphorus Vanadium-Oxide. *Chem. Rev.* **1988**, *88* (1), 55−80.

(6) Forzatti, P. Present status and perspectives in de-NOx SCR catalysis. *Appl. Catal., A* **2001**, *222* (1−2), 221−236.

(7) Ballarini, N.; Cavani, F.; Cericola, A.; Cortelli, C.; Ferrari, M.; Trifiro, F.; Capannelli, G.; Comite, A.; Catani, R.; Cornaro, U. Supported vanadium oxide-based catalysts for the oxidehydrogenation of propane under cyclic conditions. *Catal. Today* **2004**, *91-92*, 99−104.

(8) Blasco, T.; Nieto, J. M. L. Oxidative dyhydrogenation of short chain alkanes on supported vanadium oxide catalysts. *Appl. Catal., A* **1997**, *157* (1−2), 117−142.

(9) Cavani, F.; Ballarini, N.; Cericola, A. Oxidative dehydrogenation of ethane and propane: How far from commercial implementation? *Catal. Today* **2007**, *127* (1−4), 113−131.

(10) Cavani, F.; Trifiro, F. The Oxidative Dehydrogenation of Ethane and Propane as an Alternative Way for the Production of Light Olefins. *Catal. Today* **1995**, *24* (3), 307−313.

(11) Chaar, M. A.; Patel, D.; Kung, H. H. Selective Oxidative Dehydrogenation of Propane over V-Mg-O Catalysts. *J. Catal.* **1988**, *109* (2), 463−467.

(12) Chen, K. D.; Bell, A. T.; Iglesia, E. Kinetics and mechanism of oxidative dehydrogenation of propane on vanadium, molybdenum, and tungsten oxides. *J. Phys. Chem. B* **2000**, *104* (6), 1292−1299.

(13) Grabowski, R. Kinetics of Oxidative Dehydrogenation of C_2-C_3 Alkanes on Oxide Catalysts. *Catal. Rev.: Sci. Eng.* **2006**, *48* (2), 199−26.

(14) Mamedov, E. A.; Cortés Corberan, V. Oxidative Dehydrogenation of Lower Alkanes on Vanadium Oxide-Based Catalysts - the Present State-of-the-Art and Outlooks. *Appl. Catal., A* **1995**, *127* (1−2), 1−40.

(15) Nieto, J. M. L. The selective oxidative activation of light alkanes. From supported vanadia to multicomponent bulk V-containing catalysts. *Top. Catal.* **2006**, *41* (1−4), 3−15.

(16) Vilter, H. Peroxidases from Phaeophyceae: A Vanadium(V)-dependent peroxidase from Ascophyllum nodosum. *Phytochemistry* **1984**, *23* (7), 1387−1390.

(17) Bayer, E.; Kneifel, H. Notizen: Isolation of Amavadin, a Vanadium Compound Occuring in Amanita Muscaria. *Z. Naturforsch., B: J. Chem. Sci.* **1972**, *27* (2), 207.

(18) Eady, R. R.; Robson, R. L.; Richardson, T. H.; Miller, R. W.; Hawkins, M. The vanadium nitrogenase ofAzotobacter chroococcum. Purification and properties of the VFe protein. *Biochem. J.* **1987**, *244* (1), 197−207.

(19) Hales, B. J.; True, A. E.; Hoffman, B. M. Detection of a new signal in the ESR spectrum of vanadium nitrogenase from Azotobacter vinelandii. *J. Am. Chem. Soc.* **1989**, *111* (22), 8519−8520.

(20) Ishii, T.; Nakai, I.; Numako, C.; Okoshi, K.; Otake, T. Discovery of a new vanadium accumulator, the fan wormPseudopotamilla occelata. *Naturwissenschaften* **1993**, *80* (6), 268−270.

(21) Michibata, H. Molecular biological approaches to the accumulation and reduction of vanadium by ascidians. *Coord. Chem. Rev.* **2003**, *237* (1−2), 41−51.

(22) Krzystek, J.; Fiedler, A. T.; Sokol, J. J.; Ozarowski, A.; Zvyagin, S. A.; Brunold, T. C.; Long, J. R.; Brunel, L. C.; Telser, J. Pseudooctahedral complexes of vanadium(III): electronic structure investigation by magnetic and electronic spectroscopy. *Inorg. Chem.* **2004**, *43* (18), 5645−58.

(23) Robbins, D. J.; Stillman, M. J.; Thomson, A. J. Magnetic circular dichroism spectroscopy of the vanadyl ion. *J. Chem. Soc., Dalton Trans.* **1974**, 813−820.

(24) Davies, S. C.; Durrant, M. C.; Hughes, D. L.; Le Floc'h, C.; Pope, S. J. A.; Reid, G.; Richards, R. L.; Sanders, J. R. Synthesis, spectroscopic and EXAFS studies of vanadium complexes of trithioether ligands and crystal structures of $[VCl_3([9]aneS_3)]$ and $[VI_2(thf)([9]aneS_3)]$ ($[9]aneS_3$ = 1,4,7-trithiacyclononane). *J. Chem. Soc., Dalton Trans.* **1998**, 2191−2198.

(25) Dilli, S.; Patsalides, E. A convenient new Method for the preparation of vanadium(III) β-diketonates. *Aust. J. Chem.* **1976**, *29* (11), 2389−2393.

(26) Fowles, G. W. A.; Greene, P. T.; Lester, T. E. Ether complexes of tervalent titanium and vanadium. *J. Inorg. Nucl. Chem.* **1967**, *29* (9), 2365−2370.

(27) Linert, W.; Herlinger, E.; Margl, P.; Bočka, R. Spectroscopic, Electrochemical and Quantum Mechanical Investigations of Vanadyl-(IV)-Acetylacetonate in Non-Aqueous Solutions. *J. Coord. Chem.* **1993**, *28* (1), 1−16.

(28) Manxzer, L. E.; Deaton, J.; Sharp, P.; Schrock, R. R. Tetrahydrofuran Complexes of Selected Early Transition Metals. *Inorg. Synth.* **2007**, *21*, 135−139.

(29) Reynolds, J. G.; Jones, E. L.; Huffman, J. C.; Christou, G. Deoxygenation of Oxovanadium(IV) Complexes under Mild Conditions - Conversion of Vanadyl Species to the Corresponding Dihalides with Carboxylic-Acid Halides. *Polyhedron* **1993**, *12* (4), 407−414.

(30) Stoll, S.; Schweiger, A. EasySpin, a comprehensive software package for spectral simulation and analysis in EPR. *J. Magn. Reson.* **2006**, *178* (1), 42−55.

(31) Neese, F.; Solomon, E. I. MCD C-Term Signs, Saturation Behavior, and Determination of Band Polarizations in Randomly Oriented Systems with Spin $S \geq 1/2$. Applications to $S = 1/2$ and $S = 5/2$. *Inorg. Chem.* **1999**, *38* (8), 1847−1865.

(32) Neese, F. W.; Becker, Ute; Bykov, D.; Ganyushin, D.; Hansen, A.; Izsák, R.; Kollmar, C.; Kossmann, S.; Liakos, D. G.; Manganas, D.; Pantazis, D. A.; Petrenko, T.; Reimann, C.; Riplinger, C.; Risthaus, T.; Roemelt, M.; Sandhöfer, B.; Schapiro, I.; Sivalingam, K.; Wezisla, B.; Kállay, M.; Grimme, S.; Valeev, E.; Chan, G. *ORCA: An ab initio, DFT*

DOI: 10.1021/acs.inorgchem.8b00486
Inorg. Chem. XXXX, XXX, XXX−XXX

and semiempirical SCF-MO package, version 4.0; Max-Planck-Institut: Mülheim an der Ruhr, Germany, 2017.
(33) Becke, A. D. Density-functional exchange-energy approximation with correct asymptotic behavior. *Phys. Rev. A: At., Mol., Opt. Phys.* **1988**, *38* (6), 3098−3100.
(34) Perdew, J. P. Density-Functional Approximation for the Correlation-Energy of the Inhomogeneous Electron-Gas. *Phys. Rev. B: Condens. Matter Mater. Phys.* **1986**, *33* (12), 8822−8824.
(35) Schäfer, A.; Horn, H.; Ahlrichs, R. Fully optimized contracted Gaussian basis sets for atoms Li to Kr. *J. Chem. Phys.* **1992**, *97* (4), 2571−2577.
(36) Weigend, F.; Ahlrichs, R. Balanced basis sets of split valence, triple zeta valence and quadruple zeta valence quality for H to Rn: Design and assessment of accuracy. *Phys. Chem. Chem. Phys.* **2005**, *7* (18), 3297−305.
(37) Cotton, F. A.; Duraj, S. A.; Extine, M. W.; Lewis, G. E.; Roth, W. J.; Schmulbach, C. D.; Schwotzer, W. Structural Studies of the Vanadium(II) and Vanadium(III) Chloride Tetrahydrofuran Solvates. *J. Chem. Soc., Chem. Commun.* **1983**, 1377−1378.
(38) Durrant, M. C.; Davies, S. C.; Hughes, D. L.; Le Floc'h, C.; Richards, R. L.; Sanders, J. R.; Champness, N. R.; Pope, S. J.; Reid, G. Crown thioether complexes of vanadium(II), vanadium(III) and vanadium(IV): X-ray crystal structure of $[VCl_3([9]aneS_3)]$. *Inorg. Chim. Acta* **1996**, *251* (1−2), 13−14.
(39) Morosin, B.; Montgomery, H. The crystal structure of α- and β-tris(2,4-pentanedionato)vanadium(III). *Acta Crystallogr., Sect. B: Struct. Crystallogr. Cryst. Chem.* **1969**, *25* (7), 1354−1359.
(40) Silva, R. M. S. d.; Spiazzi, C. C.; Bortolotto, R.; Burrow, R. A. Redetermination of bis(acetylacetonato)oxidopyridinevanadium(IV). *Acta Crystallogr., Sect. E: Struct. Rep. Online* **2007**, *63* (9), m2422−m2422.
(41) Roos, B. O.; Taylor, P. R.; Siegbahn, P. E. M. A Complete Active Space SCF Method (CASSCF) Using a Density-Matrix Formulated Super-CI Approach. *Chem. Phys.* **1980**, *48* (2), 157−173.
(42) Siegbahn, P. E. M.; Almlof, J.; Heiberg, A.; Roos, B. O. The Complete Active Space Scf (CASSCF) Method in a Newton-Raphson Formulation with Application to the HNO Molecule. *J. Chem. Phys.* **1981**, *74* (4), 2384−2396.
(43) Angeli, C.; Cimiraglia, R.; Evangelisti, S.; Leininger, T.; Malrieu, J.-P. Introduction of n-electron valence states for multireference perturbation theory. *J. Chem. Phys.* **2001**, *114* (23), 10252−10264.
(44) Angeli, C.; Cimiraglia, R. Multireference perturbation configuration interaction V. Third-order energy contributions in the Møller−Plesset and Epstein−Nesbet partitions. *Theor. Chem. Acc.* **2002**, *107* (5), 313−317.
(45) Neese, F.; Valeev, E. F. Revisiting the Atomic Natural Orbital Approach for Basis Sets: Robust Systematic Basis Sets for Explicitly Correlated and Conventional Correlated ab initio Methods. *J. Chem. Theory Comput.* **2011**, *7* (1), 33−43.
(46) Stoychev, G. L.; Auer, A. A.; Neese, F. Automatic Generation of Auxiliary Basis Sets. *J. Chem. Theory Comput.* **2017**, *13* (2), 554−562.
(47) Neese, F. Efficient and accurate approximations to the molecular spin-orbit coupling operator and their use in molecular g-tensor calculations. *J. Chem. Phys.* **2005**, *122* (3), 34107.
(48) Hess, B. A.; Marian, C. M. In *Computational Molecular Spectroscopy*; Jensen, P. B., Ed.; Wiley: New York, 2000; p 169ff.
(49) Cahier, B.; Maurice, R.; Bolvin, H.; Mallah, T.; Guihéry, N. Tools for Predicting the Nature and Magnitude of Magnetic Anisotropy in Transition Metal Complexes: Application to Co(II) Complexes. *Magnetochemistry* **2016**, *2* (4), 31−45.
(50) Roos, B. O.; Malmqvist, P.-Å. Relativistic quantum chemistry: the multiconfigurational approach. *Phys. Chem. Chem. Phys.* **2004**, *6* (11), 2919−2927.
(51) Durand, P.; Malrieu, J.-P. In *Advances in Chemical Physics: Ab Initio Methods in Quantum Chemistry*; Lawley, K. P., Ed.; John Wiley & Sons Ltd.: Hoboken, NJ, 1987; Vol. *67*, Part 1, pp 321−412.
(52) Atanasov, M.; Ganyushin, D.; Sivalingam, K.; Neese, F. A Modern First-Principles View on Ligand Field Theory Through the Eyes of Correlated Multireference Wavefunctions. *Struct. Bonding* **2011**, *143*, 149−220.
(53) Atanasov, M.; Zadrozny, J. M.; Long, J. R.; Neese, F. A theoretical analysis of chemical bonding, vibronic coupling, and magnetic anisotropy in linear iron(II) complexes with single-molecule magnet behavior. *Chem. Sci.* **2013**, *4* (1), 139−156.
(54) Adamsky, H. *AOMX program*; Institut für Theoretische Chemie, Heinrich-Heine-Universität Düsseldorf: Düsseldorf, Germany, 1996.
(55) Ballhausen, C. J.; Gray, H. B. The Electronic Structure of the Vanadyl Ion. *Inorg. Chem.* **1962**, *1* (1), 111−122.
(56) Jørgensen, C. K.; Döger, S.; Frydman, M.; Sillén, L. G. Comparative Ligand Field Studies. IV. Vanadium(IV), Titanium(III), Molybdenum(V), and other Systems with one d-Electron. *Acta Chem. Scand.* **1957**, *11*, 73−85.
(57) Furlani, C. Sull'origine della banda di assorbimento nello spettro visibile dello ione VO^{2+}. *Ricerca sci.* **1957**, *27*, 1141−1145.
(58) Kuska, H. A.; Rogers, M. T. Assignment of Optical Spectra for Vanadyl Complexes. *Inorg. Chem.* **1966**, *5* (2), 313−315.
(59) Dodge, R. P.; Templeton, D. H.; Zalkin, A. Crystal Structure of Vanadyl Bisacetylacetonate. Geometry of Vanadium in Fivefold Coordination. *J. Chem. Phys.* **1961**, *35* (1), 55−67.
(60) Bernal, I.; Rieger, P. H. Solvent Effects on the Optical and Electron Spin Resonance Spectra of Vanadyl Acetylacetonate. *Inorg. Chem.* **1963**, *2* (2), 256−260.
(61) Walker, F. A.; Carlin, R. L.; Rieger, P. H. ESR Studies of Coordination to the Sixth Position of Vanadyl Acetylacetonate. *J. Chem. Phys.* **1966**, *45* (11), 4181−4189.
(62) Selbin, J.; Maus, G.; Johnson, D. L. Spectral studies of β-ketoenolate complexes of oxovanadium(IV). *J. Inorg. Nucl. Chem.* **1967**, *29* (7), 1735−1744.
(63) Selbin, J.; Holmes, L. H.; McGlynn, S. P. Electronic structure, spectra and magnetic properties of oxycations—IV ligation effects on the infra-red spectrum of the vanadyl ion. *J. Inorg. Nucl. Chem.* **1963**, *25* (11), 1359−1369.
(64) Basu, G.; Yeranos, W.; Belford, R. L. Structure in the Electronic Spectra of Vanadyl Acetylacetonate. *Inorg. Chem.* **1964**, *3* (6), 929−931.
(65) O'Connor, C. J. Magnetochemistry—Advances in Theory and Experimentation. *Prog. Inorg. Chem.* **2007**, *29*, 203−283.
(66) Gregson, A. K.; Doddrell, D. M.; Healy, P. C. Low-temperature magnetic properties of three vanadium(III) and manganese(III) β-diketonate complexes. *Inorg. Chem.* **1978**, *17* (5), 1216−1219.
(67) de Laeter, J. R.; Böhlke, J. K.; De Bièvre, P.; Hidaka, H.; Peiser, H. S.; Rosman, K. J. R.; Taylor, P. D. P. Atomic weights of the elements. Review 2000 (IUPAC Technical Report). *Pure Appl. Chem.* **2003**, *75* (6), 683−800.
(68) Machin, D. J.; Murray, K. S. The magnetism and spectra of some octahedral vanadium(III) complexes. *J. Chem. Soc. A* **1967**, 1498−1504.
(69) Piper, T. S.; Carlin, R. L. Crystal Spectra of Some Trisacetylacetonates. *Inorg. Chem.* **1963**, *2* (2), 260−263.
(70) Lalancette, R. A.; Arslan, E.; Bernal, I.; Willhelm, D.; Grebowicz, J.; Pluta, M. The thermochemistry and crystallography of the metal tris-acetylacetonates. *J. Therm. Anal. Calorim.* **2018**, *131* (3), 2809−2819.
(71) Arslan, E.; Lalancette, R. A.; Bernal, I. An historic and scientific study of the properties of metal(III) tris-acetylacetonates. *Struct. Chem.* **2017**, *28* (1), 201−212.
(72) Van Kuiken, B. E.; Hahn, A. W.; Maganas, D.; DeBeer, S. Measuring Spin-Allowed and Spin-Forbidden d-d Excitations in Vanadium Complexes with 2p3d Resonant Inelastic X-ray Scattering. *Inorg. Chem.* **2016**, *55* (21), 11497−11501.
(73) Griffith, J. S. *Theory of Transition Metal Ions*; Cambridge University Press: New York, 1961; p 302.
(74) Tregenna-Piggott, P. L. W.; Best, S. P. Single-Crystal Raman Spectroscopy of the Rubidium Alums $RbM^{III}(SO_4)_2{\cdot}12H_2O$ (M^{III}= Al, Ga, In, Ti, V, Cr, Fe) between 275 and 1200 cm^{-1}: Correlation between the Electronic Structure of the Tervalent Cation and Structural Abnormalities. *Inorg. Chem.* **1996**, *35* (19), 5730−5736.

DOI: 10.1021/acs.inorgchem.8b00486
Inorg. Chem. XXXX, XXX, XXX−XXX

(75) Orgel, L. E. Double Bonding in Chelated Metal Complexes. *J. Chem. Soc.* **1961**, 3683−3686.
(76) Ceulemans, A.; Dendooven, M.; Vanquickenborne, L. G. The ligand field of phase-coupled ligators. *Inorg. Chem.* **1985**, *24* (8), 1153−1158.
(77) Selbin, J. The Chemistry of Oxovanadium(IV). *Chem. Rev.* **1965**, *65* (2), 153−175.

DOI: 10.1021/acs.inorgchem.8b00486
Inorg. Chem. XXXX, XXX, XXX−XXX